1 Introduction

Beneath the Arctic ocean lie vast quantities of untapped oil and natural gas reserves. The U.S Geological Survey (USGS) estimates that the region is home to 13% of world's undiscovered oil reserves, and 30% of world's untapped natural gas reserves [7]. The tight global energy market coupled with the existence of such large reservoirs have peeked interest of the neighboring countries in exploration of the reserves.

Recovery of the oil and gas from reserves that lie beneath the sea require construction of marine pipelines which partly will be submerged beneath the sea surface with long spans supported on the seabed. Exposure of the pipes to the environment leads to both man-made and geo-environmental hazards such as dragging of anchors and cables, thermal buckling, strudel scouring of seabed, and gouging by ice masses. Although pipelines are more inflexible when compared to alternatives of fluid transportation in tanks, they entail lower operating costs and a lifetime of at least 40 years [24].

The seabed scouring process (also referred to as seabed gouging, furrowing, plowing, scoring, scarping, etc) describes the physical interaction that takes place when ice masses come in contact with the seabed. The interaction produces long gouges and basin-shaped depressions on the seabed. These are marked features of the shallow marine shelves [21, 5]. Scouring, however, is not limited to water depths corresponding to fast ice (up to 27 m). Evidence of the phenomenon is visible in water depths of 100m and more [13].

Gouging events were first discovered in the early 1970s during sonar scans of the Canadian Beaufort Sea (see [35], Chapter 2). The depths of these gouges were on average up to 2.5 meters with maximum recorded gouge depths of 4.5 meters. A more recent study of Canadian Beaufort Sea reported average gouges with depths of 0.3 meters [10], while in [13], the statistical averaging of data collected during a mapping survey conducted on the Grand Banks in 2004 revealed a mean trench depth of 0.3 meters and width of 31 meters. According to these reports, trenches do not frequently exceed in depths of 1 meter, and gouges with depths exceeding 1 meter are considered "extreme events" [2].

When ice masses come in contact with the seabed, they may continue the scouring process for several kilometers, with a preferred orientation [10, 35], or in other in-

stances, alternately impacting and rotating free of the seabed [3], producing series of craters on the seabed. It is generally accepted that the most significant risk to pipelines in this region are due to effects such ice-features [2]. The forces that the ridges apply in deeper gouges was estimated to be range $1,000 - 10,000$ tons in [25], making pipelines vulnerable to severe damage should they come in contact with the ice masses. The burial of the pipelines within the seabed is deemed to provide the ideal protection of the pipes against coming in contact with foreign objects [24].

In [25], the seabed response to gouging by ice masses was qualitatively categorized as three types (see Figure 1.1):

1. Zone I: This is the zone that the ridge actively comes in direct contact with the soil, resulting in large plastic deformation of the soil. Soil particles are first push upward forming a soil-mound in front of the soil, and subsequently pushed to the sides forming the side berms (see Figure 1.2).
2. Zone II: In this region, the soil does not come in direct contact with the ice mass, but still undergoes large plastic deformation due to large shear forces created by the ice mass.
3. Zone III: The soil behaves elastically in this region, making it the safest place to bury pipelines.

Although pipelines are safest in Zone III, the high cost of installation of the pipes in this zone makes this choice impractical. Instead, it is preferable to have the pipes buried in Zone II to protect them from coming in direct contact with ridges while at the same time, prevent excessive pipeline deformation due to large shearing forces created by the ice masses.

The typical speed of ice masses is thought to be 0.1m/s [26], with mean scour rates of 2.2×10^{-8} $\mathrm{m}^{-2}\mathrm{s}^{-1}$ [13]. Due to the large loading rates the soil experiences, it is assumed to be loaded in an undrained condition and the continued shear deformation of the soil takes place without any change in void ratio or any increase in pore-water pressure [26]. The present study relies on this premise as will be further discussed in Section 2.

Although evidence of scouring was first observed over four decades ago, there is limited amount of information available on the active scouring process in the open literature.

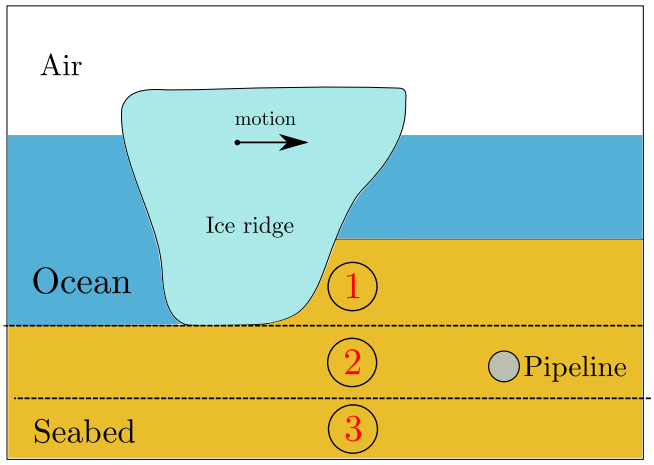

Figure 1.1: Seabed zones distinguished in [25].

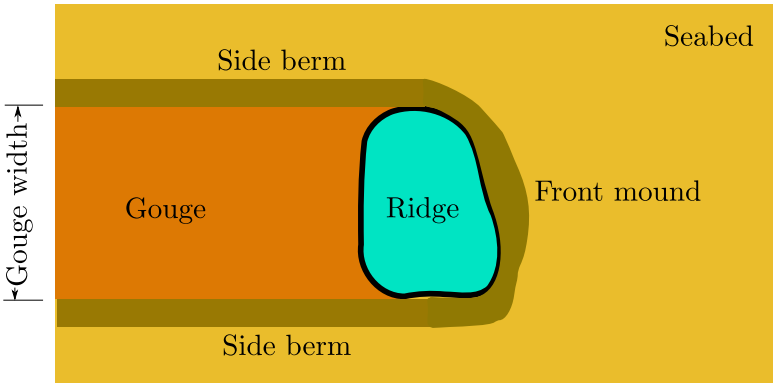

Figure 1.2: Seabed scour view from above.

The ice scouring experiments performed in laboratory settings in [6, 1] and the in-situ ice-ridge scour done in [16] are some of the few well-documented and publicly available papers on active scouring processes.

Early efforts of studying and gaining insight into the scouring process by ice masses have resorted to considering basic failure modes and equilibrium of soil and ice ridges (see e.g. [25, 6]). More recently, especially the past decade, there has been increased interest in employing advanced numerical methods for gaining insight into this complex phenomena. Despite the maturity of computational solid mechanics (CSM) and the successfully proven approaches of modeling soil as a porous medium, numerical modeling of complex phenomena such as the seabed scouring still faces difficulties. The two predominant difficulties of taking the conventional approach are the interaction between a rigid object, such as an ice-mass and the soil, and the subsequent large deformation (gouge) induced on and in the soil in the course of such interaction.

The use of arbitrary Lagrangian-Eulerian (ALE) techniques (see e.g. [11, 12]) has been extensively used in the last four decades for solution of free-surface flow problems (see e.g. [33, 17]), fluid-structure interaction (FSI) problems (see e.g. [4, 37]), and even in computational solid mechanics involving large deformations (see e.g. [8, 31]). The use of ALE methods has become a standard part of major commercially available packages for solving fluid-structure interaction and large deformation analysis. Previous numerical modeling of seabed gouging has been performed with commercially available packages such as LS-DYNA (see e.g. [14, 15]) and ABAQUS (see e.g. [23, 27]). In such studies, the large deformation in the seabed is accommodated using ALE techniques combined with re-meshing.

Re-meshing techniques are computationally expensive and their extension to three-dimensional analysis is far from trivial. In addition to the high computational cost, the regeneration of computational domains requires remapping of variables between a hierarchy of meshes, which may possess the added disadvantage of deterioration, and in extreme cases, lack of convergence to a solution of the nonlinear equations.

In these methods, the object is tracked in a Lagrangian fashion, while the fluid computational domain is allowed to deform and warp such that conformity of meshes between the fluid and the object is maintained. Such procedures where a body-fitted mesh discretization evolves with the rigid-object's motion, suffer from the same issues present in Lagrangian tracking of the soil-object interface: in problems where the body is subject to large displacements and rotations, there is still need for compu-

tationally expensive re-meshing of the domain of interest, and inevitably remapping of variables between meshes.

More recently, [32] described the use of Particle-in-Cell method (PIC) ([9]) for two-dimensional analysis of the large-displacement gouging process. In this work, we present an alternative approach for the numerical modeling of the soil gouging process by treating the soil as a highly viscous non-Newtonian fluid, thereby converting deformation to viscous flow.

The contact problem and re-meshing requirements used in classical modeling approaches can be avoided by recasting the soil-object interaction (SOI) as a fluid-object interaction (FOI) problem. The idea of approximating soil behavior as a highly viscous non-Newtonian fluid was successfully tested in [28] for numerical modeling of torpedo anchor installations in seabeds using a finite-volume based commercially available computational-fluid-dynamics (CFD) software. The large rigid-body displacement of the torpedo anchor, modeled as a rigid-object, was accommodated using frequent re-meshing of the computational domain.

In this work, we continued this idea of approximating saturated soil as an incompressible viscous fluid, and generalized the formulation to soil-structure/object interaction in a large-deformation framework. Within this approach, the soil-ridge and the soil-pipe interactions are treated as fluid-object and fluid-structure interaction problems, respectively. The arbitrarily large topological changes in the soil are accommodated by representing the water-soil interface as a single dynamic implicit surface.

2 Constitutive Model for Soil and Fluid

We express the Cauchy stress tensor $\boldsymbol{\sigma}^f$ for both the soil and water through the use of the following simple general nonlinear constitutive equation given by

$$\boldsymbol{\sigma}^f = 2\mu^f(\dot{\gamma})\,\dot{\boldsymbol{\epsilon}} - p\boldsymbol{I}, \tag{2.1}$$

$$\dot{\boldsymbol{\epsilon}} = \nabla^s_{\boldsymbol{x}}\boldsymbol{v}^f - \frac{1}{3}\left(\nabla_{\boldsymbol{x}}\cdot\boldsymbol{v}^f\right)\boldsymbol{I}, \tag{2.2}$$

$$\dot{\gamma} = \sqrt{2\dot{\boldsymbol{\epsilon}} : \dot{\boldsymbol{\epsilon}}}, \tag{2.3}$$

where, $\dot{\boldsymbol{\epsilon}}$ is the strain-rate tensor, $\nabla^s_{\boldsymbol{x}}$ is the symmetric spatial gradient operator, μ^f is the dynamic viscosity of the fluids, and $\dot{\gamma} \in [0, \infty)$ is a measure of the strain-rate tensor. In the definition of the strain-rate tensor, in addition to the spherical part, we choose to retain the deviatoric portion since it is not identically zero on the discrete level.

Following [28], we employ the Herschel-Bulkley constitutive model for approximating the behavior of soil as a fluid. The Herschel-Bulkley model combines the Bingham plastic model for modeling the plastic forces along with the power-law model to simulate the strain-rate effect in soil. The Herschel-Bulkley model as a function of strain-rate can be stated as

$$\mu(\dot{\gamma}) = \begin{cases} \frac{\tau_0}{\dot{\gamma}_0} & \dot{\gamma} \leq \dot{\gamma}_0 \\ \frac{\tau}{\dot{\gamma}} & \dot{\gamma} > \dot{\gamma}_0 \end{cases}, \tag{2.4}$$

$$\tau = \tau_0 \left[1 + \lambda_{hb} \log_{10} \left(\frac{\dot{\gamma}}{\dot{\gamma}_0} \right) \right], \tag{2.5}$$

where τ_0, $\dot{\gamma}_0 \in (0, \infty)$ are the maximum stress and strain-rates the fluid experiences in the linear regime, respectively, and $\lambda_{hb} \in [0, \infty)$ is a dimensionless softening parameter, with $\lambda_{hb} = 0$ representing a elastic-perfectly-plastic material. The effect of this parameter on the stress level is highlighted in Figure 2.1.

In [28], the softening coefficient λ_{hb} was calibrated at 0.1 on the basis of laboratory anchor installation tests performed in [34], and the yield shear strain-rate of the soil was assumed to be 0.024 1/s, consistent with the yield shear strain-rate in a vane shear test used for determining the undrained strength of the soil. In this paper, we use these properties, and further assume that the yield shear-stress is uniform throughout the domain. It is important to note that while this model simulates reduction in the shear strength of soil, it is not history-dependent, and cannot predict local hardening and softening of soil as predicted by soil plasticity models.

2.1 Validation

In order to demonstrate the capability of the numerical framework adopted herein with soil represented as a viscous fluid, we consider the penetration of a rigid cylinder

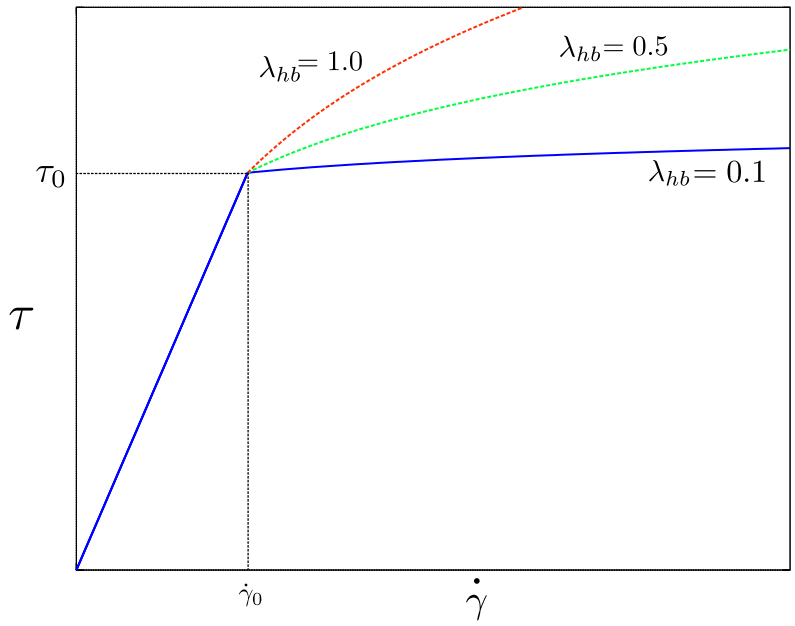

Figure 2.1: Soil constitutive model with selected values of λ_{hb}.

into soil. Both analytical plasticity solutions and experimental results are available for this problem.

We consider the vertical penetration of a rigid cylinder in cohesive soil. Both numerical and experimental data are available for this problem. Upper-bound and lower-bound plasticity analytical solutions for the bearing capacity of a wished-in-place (WIP) rigid-cylinder in a perfectly plastic full and half-space have been studied (see e.g. [22, 18, 29]). In the WIP plasticity solutions, the surface heave formed during the penetration of the pipe is ignored. Computational results for the WIP problem were presented in [20], and in [19] the effect of surface heave on the resistance of put-in-place (PIP) pipes has been studied computationally. Experimental results for the same problem have been reported in [36].

The soil profile and soil resistance on cylinder after embedment by half a cylinder diameter is shown in Figure 2.2.

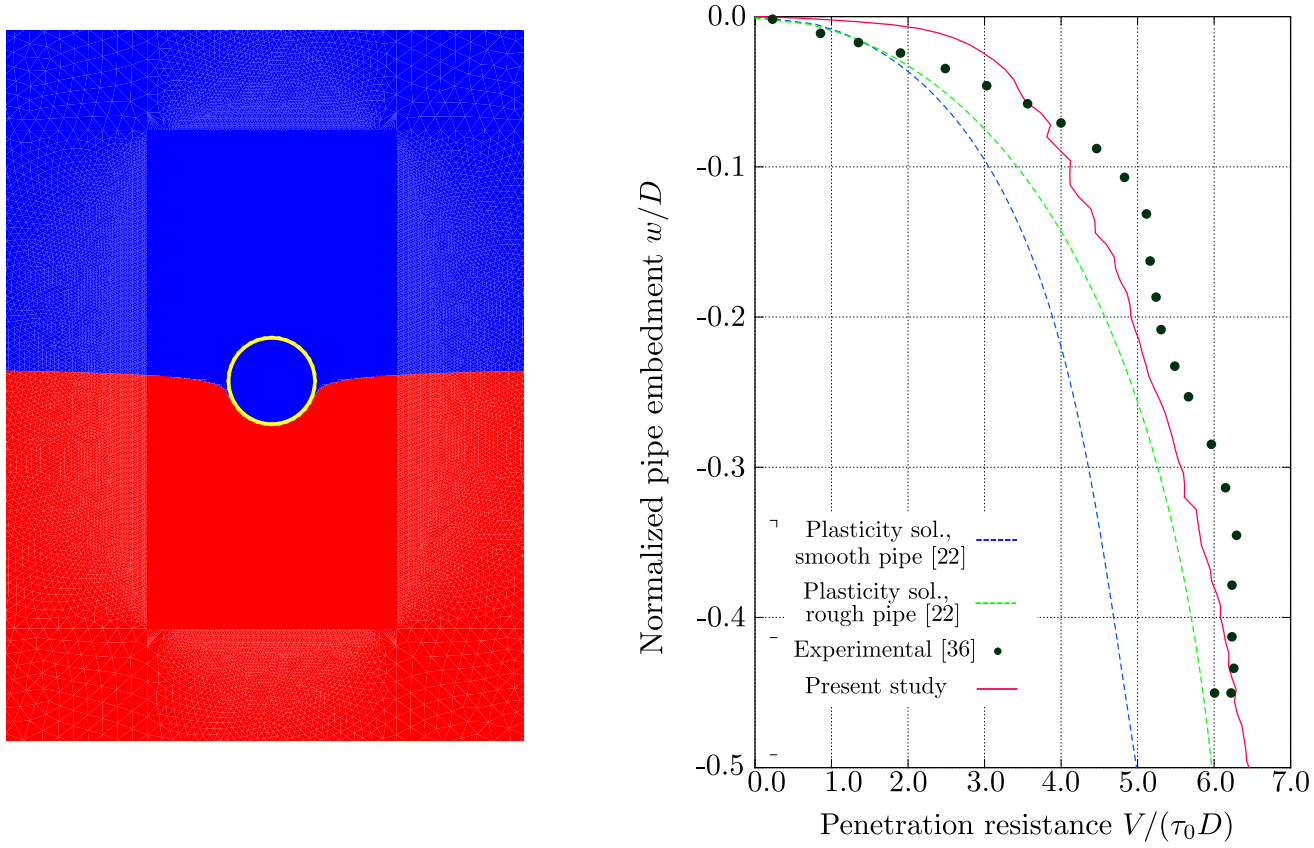

Figure 2.2: Penetration of a rigid cylinder into soil. left: profile of soil after penetration. right: normalized resistance versus embedment depth.

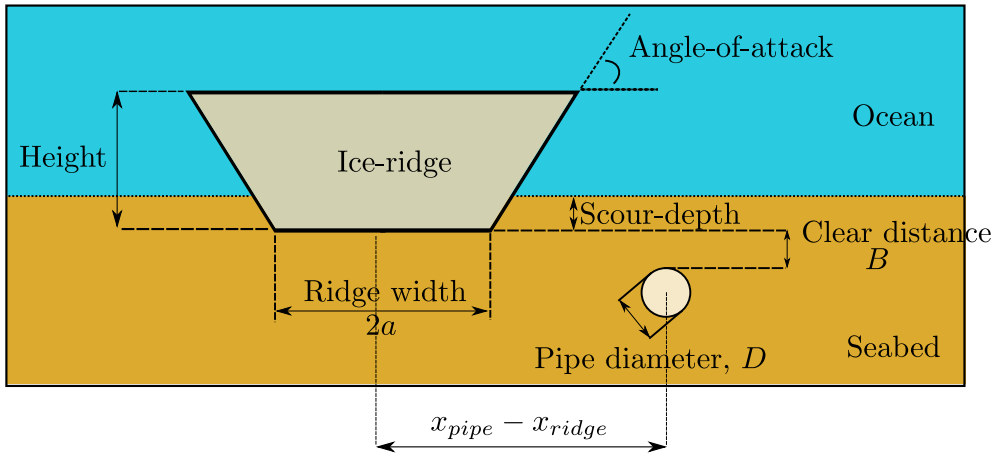

Figure 3.1: Schematics view of ridge and notations.

3 Seabed Gouging Computational Model

The computational model for the two-dimensional analyses (Section 4) is a rectangular box of dimensions $[135 \times 25]$ m^2. The pipe considered is 24 inches in diameter and it is centered at $(81.25\text{m}, 8.7\text{m})$. The computational model for the "two-and-a-half" (Section 5) dimensional analyses is $[135 \times 42]$ m^2 with either an 18- or a 24-inch pipe centered at $(81\text{m}, 20.61\text{m})$.

The ridge, modeled as a rigid object moving with a prescribed velocity $\boldsymbol{v}_o$, has a base of 10 m, with an attack angle of 33°. The ridge is initially positioned such that its base center is -49.25m away from the center line of the pipe, in effect, starting two ridge-width apart from the pipeline. In all analysis, the ridge is assumed to be fully submerged in the water to avoid inclusion of the ocean-atmosphere interface.

The ocean water is modeled as an incompressible Newtonian fluid with a mass density of 1000 kg/m^3, with a dynamic viscosity of 0.001 kg/m· s. No special attention is paid to the turbulence that may take place in water in order to save on computational resources.

The soil mass density in all studies is assumed to be 1400 kg/m^3. The pipeline is modeled as elastic with a linear elastic modulus of $E_p = 210$ GPa. In the two-and-

a-half dimensional stress analysis, the pipeline's yield stress is assumed to be 358.5 MPa.

The initial gouge profile and embedment of the ridge are such that the ridge is exposed to soil in the direction of its motion (see Figure 1.1 for an schematic view). Slip conditions are imposed on the lateral and the top walls ($\boldsymbol{v}^f \cdot \boldsymbol{n} = 0$), and no-slip condition is imposed on the bottom wall ($\boldsymbol{v}^f = \boldsymbol{0}$) of the domain. Also, no-slip conditions are imposed on the ridge and the pipe

4 Seabed Gouging in 2-Dimensions

As two extreme cases, we consider two scenaria for the two-dimensional analysis: artificially fixed pipe in space, and a floating pipe. For both cases, we consider a soil with shear strength of 1.725 kPa, and a ridge moving at speed of 0.2 m/s with gouge depth of 1 meter. The time-history of the forces acting on the pipe relative to the location of the ridge are shown in Figure 4.1.

The oscillations in the forces are only numerical, caused predominantly by the coarseness of the mesh and the smearing of the fluid and soil properties within a transition zone.

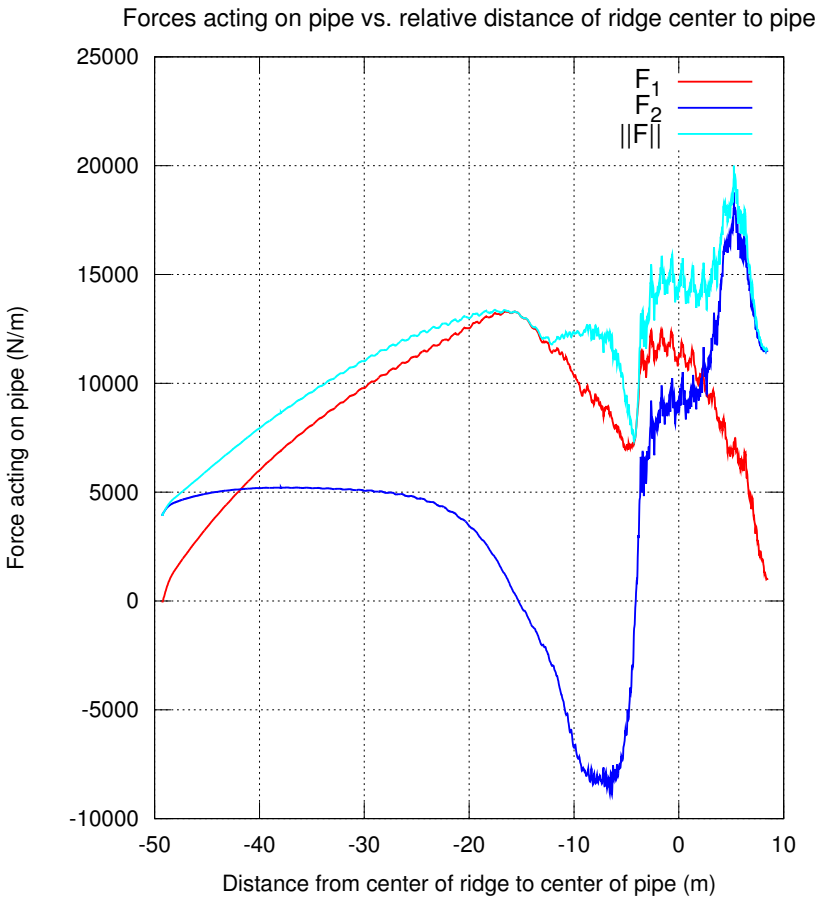

Figure 4.1: Components of forces acting on the fixed pipe.

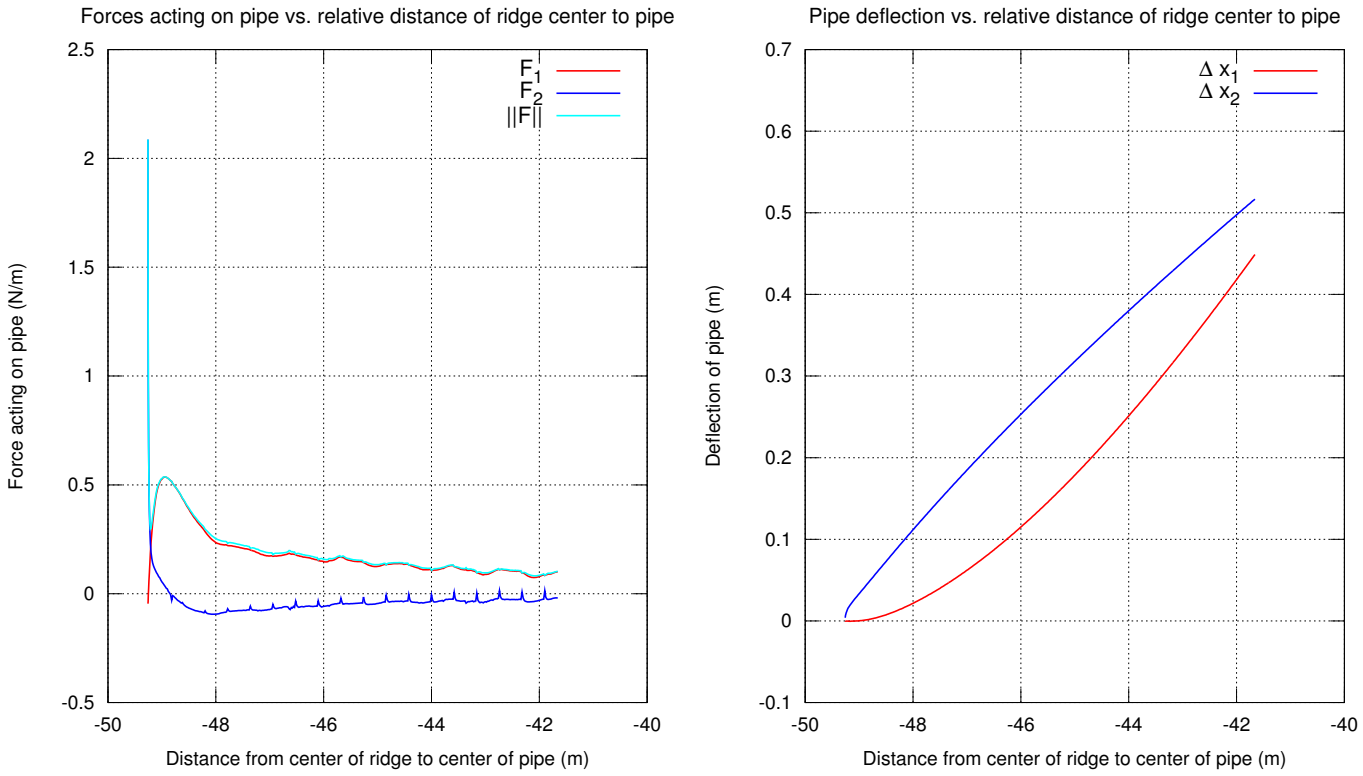

Figure 4.2: Forces (left) and pipe deflections (right) for the floating pipe.

As the second extreme case, we consider a free floating pipe with no imposed Dirichlet boundary conditions on the cross-section of the pipe. In the case of a free-floating pipe, the inertia of the pipe and the viscosity of the surrounding fluid (soil) render the problem non-singular. We consider this case as an extreme case, where the stiffness of the pipe, out-of-plane soil resistance, and the *strain*(displacement)-driven resistance of the soil are ignored due to modeling the soil as a viscous fluid. In fact, the only resistance provided to deformation (rigid or elastic) of a floating pipe is due to the *flow* (i.e. viscosity) of the fluid (soil).

The pipe forces and the deflection of a floating pipe are shown in Figure 4.2. It can be observed in this figure that the pipe undergoes half a meter of vertical and lateral translation when the center of ridge is 42 meters away from the pipeline. The analysis is terminated early in this case as this large displacement of the pipeline was deemed unreasonable and the computational mesh surrounding the pipeline was becoming exceedingly distorted.

The large vertical motion of the pipeline can be attributed to the buoyancy force acting on the pipe, which would be offset by the self-weight of the pipe when the pipe is embedded in the soil by over half of its diameter. In fact, within the time-frame that this analysis was considered, it was observed that the pipe mostly underwent rigid-body translation with rotations of about 0.3 degrees, and an out-of-plane moment (torque) in orders of magnitude of $10^{-5}\,\mathrm{N}\cdot\mathrm{m}$.

5 Coupled Soil-pipe Interaction in "2.5-Dimensions"

The resistance offered by out-of-plane soil has been neglected in the two-dimensional analyses considered in the previous section. In this section, in addition to the flow induced viscous forces, discrete linear springs are added to the pipe to simulate the out-of-plane resistance offered by soil. Furthermore, we neglect the small deformation of the pipe, and consider it undergoing rigid-body translation to facilitate introduction of springs (one in each direction) pipe now modeled as a rigid circular section. Through this approach, which will be referred to as "2.5 dimensional analysis", we estimate the three-dimensional behavior while avoiding the very time-consuming 3-dimensional computing resources required.

5.1 Effective soil stiffness

The resistance offered by out-of-plane soil in response to *deformation*, K_{soil}, is approximated by employing empirical force-displacement relations (aka p-y curves, see e.g. [30]) proposed to correlate the lateral capacity of piles to soil strength.

Consider an elastic beam of infinite length supported on an elastic two-way (linear) foundation subject to a constant load over length $2a$ (Figure 5.1). Then, the beam's deformation can be analytically computed to be

$$u_1(x) = \frac{w}{24EI}x^4 + A_1x^2 + A_2, \quad 0 \le x \le a \tag{5.1}$$

$$u_2(x) = -\frac{2\beta}{k_s}\left(P_1 D_{\beta x} + \beta M_1 C_{\beta x}\right), \quad a \le x < \infty \tag{5.2}$$

where,

$$\beta = \left(\frac{k}{4EI}\right)^{1/4}, \tag{5.3}$$

$$D_{\beta x} = e^{-\beta(x-a)}\cos\left(\beta(x-a)\right) \tag{5.4}$$

$$C_{\beta x} = e^{-\beta(x-a)}\left[\cos\left(\beta(x-a)\right) - \sin\left(\beta(x-a)\right]\right. \tag{5.5}$$

$$P_1 = -wa, \tag{5.6}$$

$$M_1 = -2EIA_1 - \frac{w}{2}a^2, \tag{5.7}$$

$$A_1 = -\frac{1}{2a + \frac{8\beta^3 EI}{k}}\left[\frac{2\beta^2 a}{k}w\left(\beta a + 1\right) + \frac{w}{6EI}a^3\right], \tag{5.8}$$

$$A_2 = -\frac{2\beta}{k_s}\left(P_1 + \beta M_1\right) - A_1a^2 - \frac{w}{24EI}a^4 \tag{5.9}$$

The midpoint displacement of beam then is

$$u_0 := u(0) = A_2 = -\frac{2\beta}{k_s}\left(P_1 + \beta M_1\right) - A_1a^2 - \frac{w}{24EI}a^4 \tag{5.10}$$

and bending moment of

$$M_0 = 2EIA_1. \tag{5.11}$$

Then, the equivalent soil resistance due to displacement (as opposed to viscous flow) is approximated as

$$K_{soil} = \frac{wL}{u_0} \tag{5.12}$$

where k_s is determined from p-y curves. In this work, we assume that the loaded length of the pipe, i.e. $2a$, is equal to the base of the ridge.

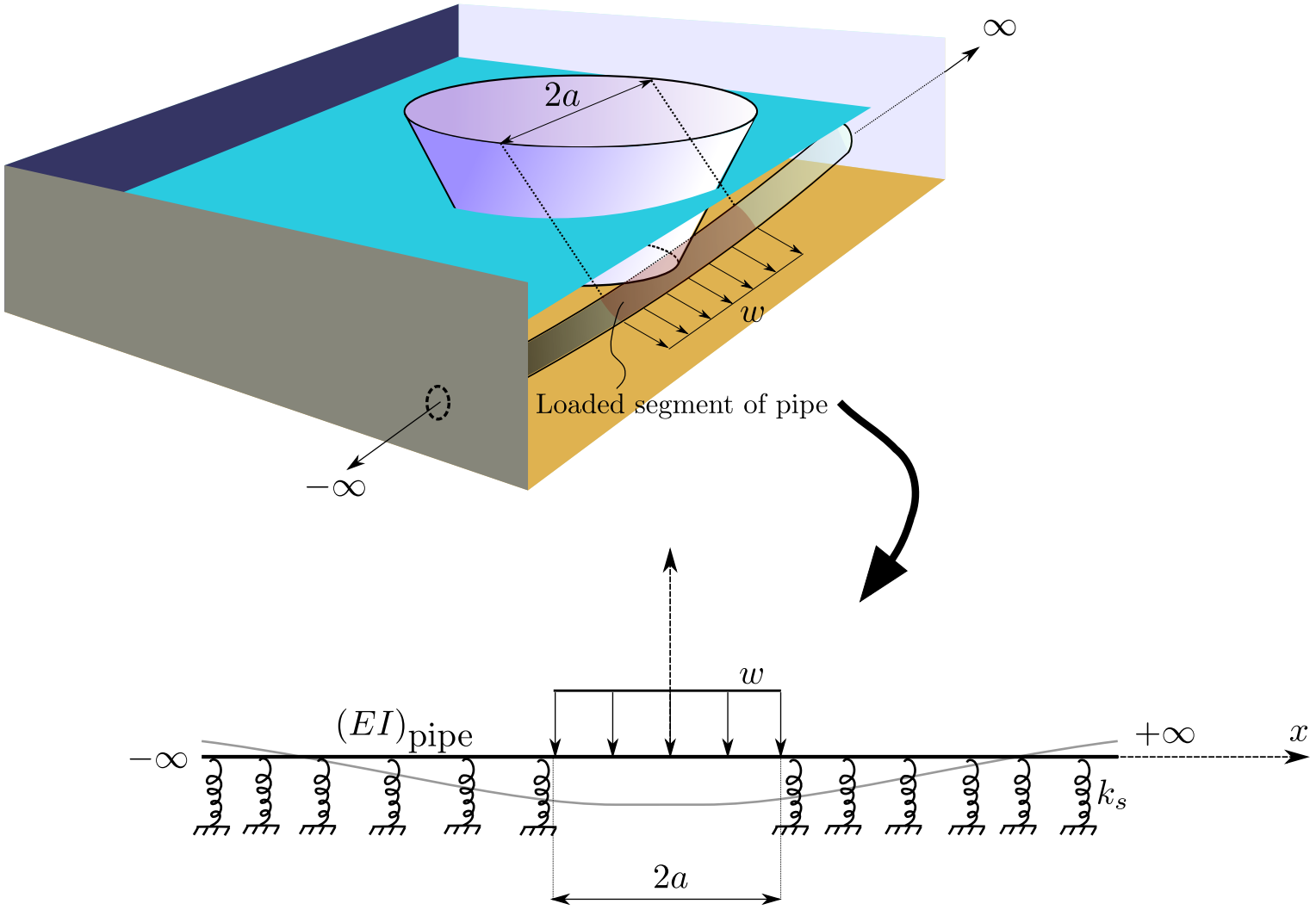

Figure 5.1: Finite distributed load of magnitude w on an infinite elastic foundation.

Table 5.1: List of cases considered for the 2.5 dimensional analysis of the seabed gouging problem.

Group	τ_0 (kPa)	v_0 (m/s)	D (in)
1	12.5	0.1	18
2	12.5	1.0	18
3	25.0	0.1	18
4	25.0	1.0	18
5	12.5	0.1	24
6	12.5	1.0	24
7	25.0	0.1	24
8	25.0	1.0	24

5.2 Parametric study

Incorporating information from the out-of-plane soil and pipe into the analysis, a parametric study of the coupled ridge-seabed-pipe interaction is performed. We consider 8 groups (Table 5.1). Each group considered considers four different clear pipe burial depth of 0.5, 1, 2, and 2.5 pipe diameters (see Figure 3.1).

The displacements and forces acting on the pipe relative to location of the ridge are shown in Figures 5.2-5.16. In these figures pipe stresses normalized by the yielding pipe stress ($\sigma_y = 358.5$ MPa) computed from Eq. (5.11) are also shown. Analyses are run until ridge goes past beyond the buried pipeline. In cases where the computed pipe stress clearly exceeds the yield stress ($\sigma/\sigma_y > 1$), the analysis are terminated. The resultant forces on ridges are processed through a zero-phase digital filtering with (10 Hz low-pass Butterworth filter).

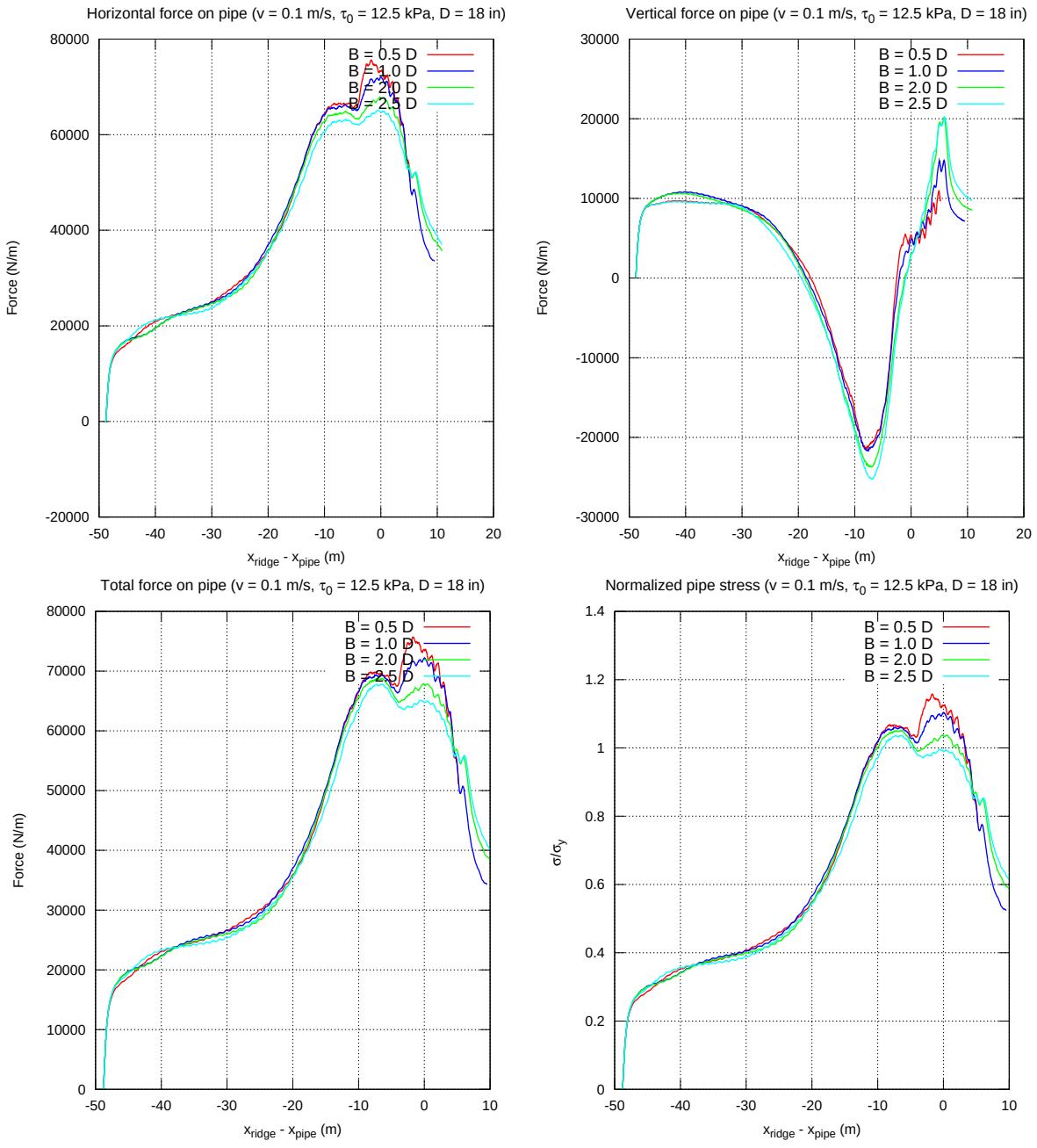

Figure 5.2: Group 1 – Forces and stresses acting on pipe

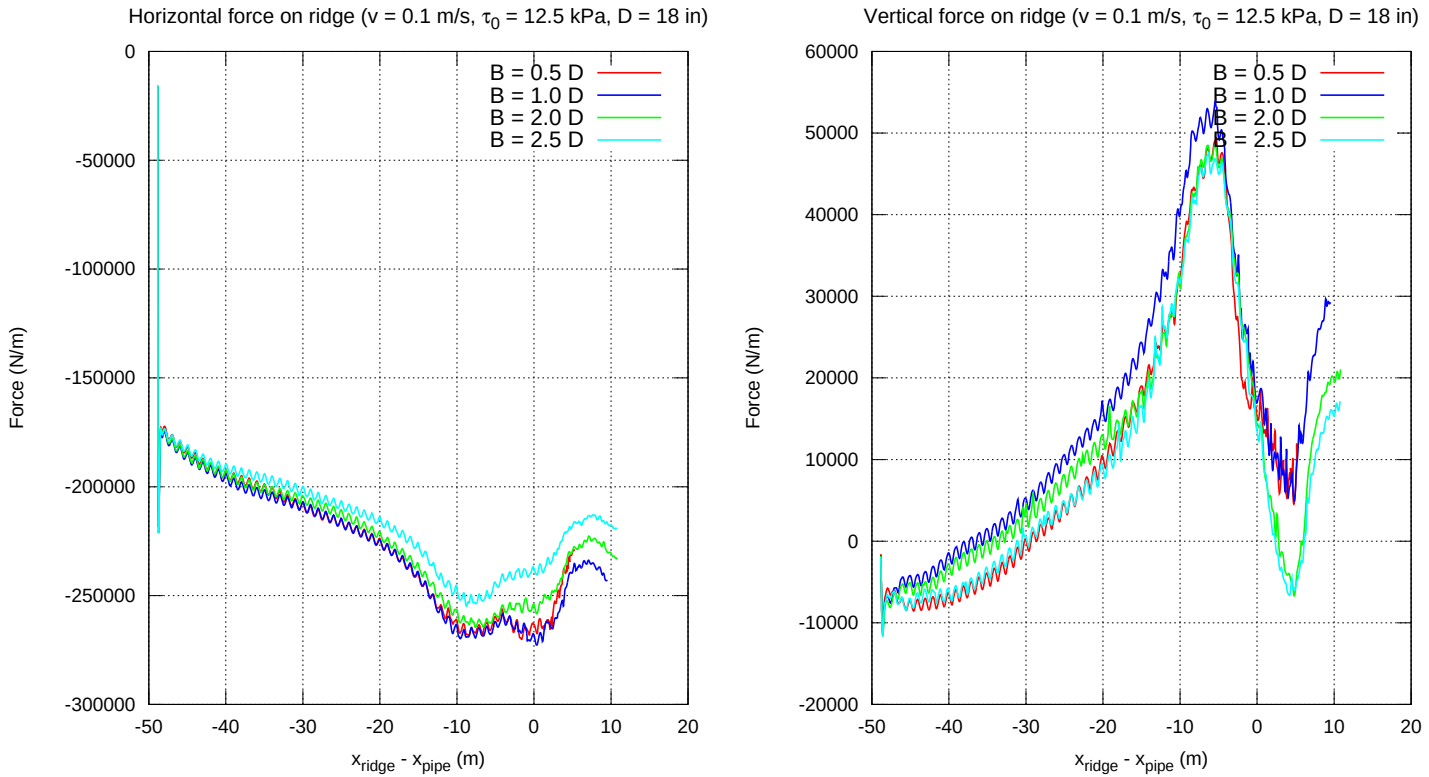

Figure 5.3: Group 1 – Forces acting on ridge

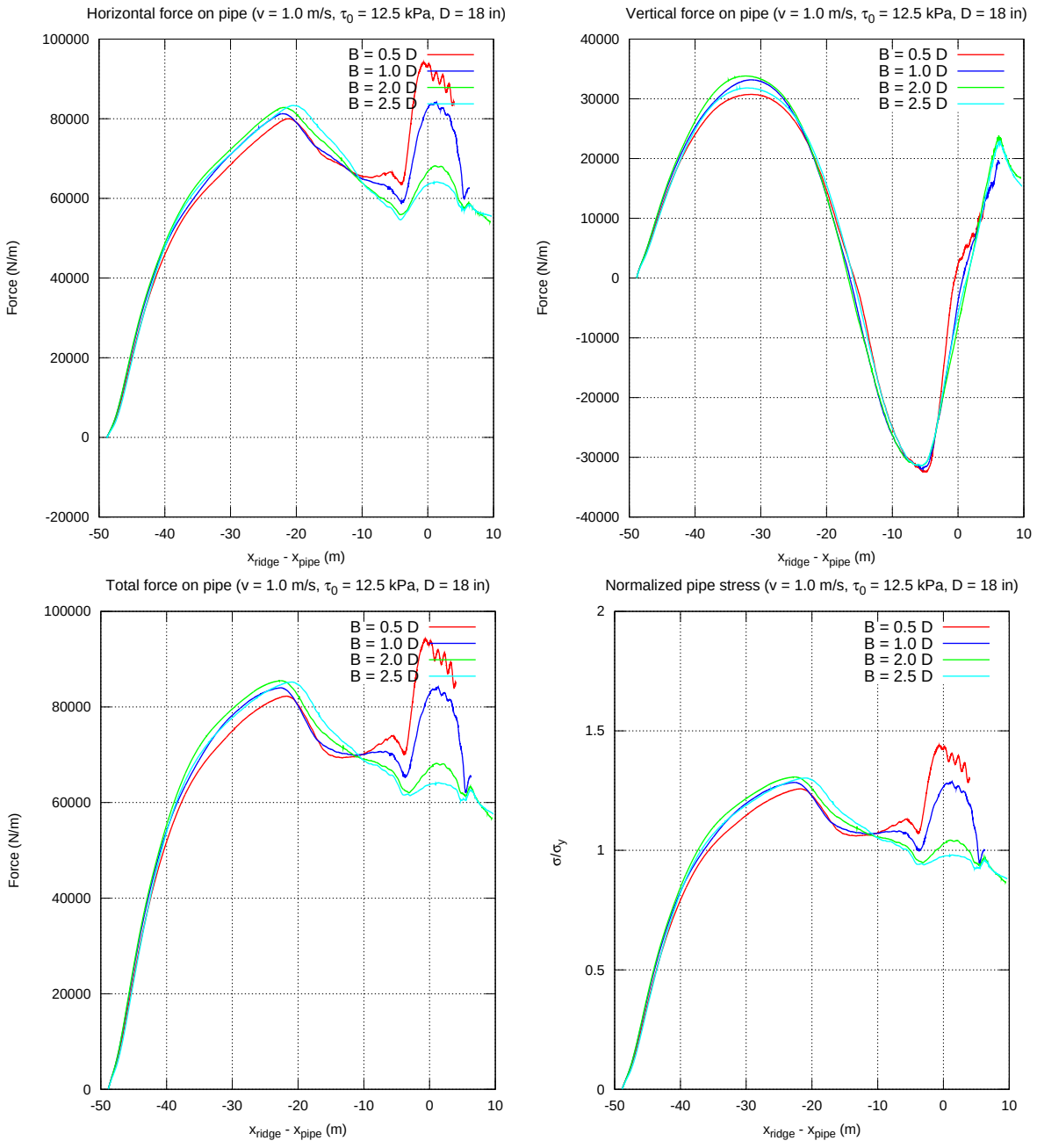

Figure 5.4: Group 2 – Forces and stresses acting on pipe

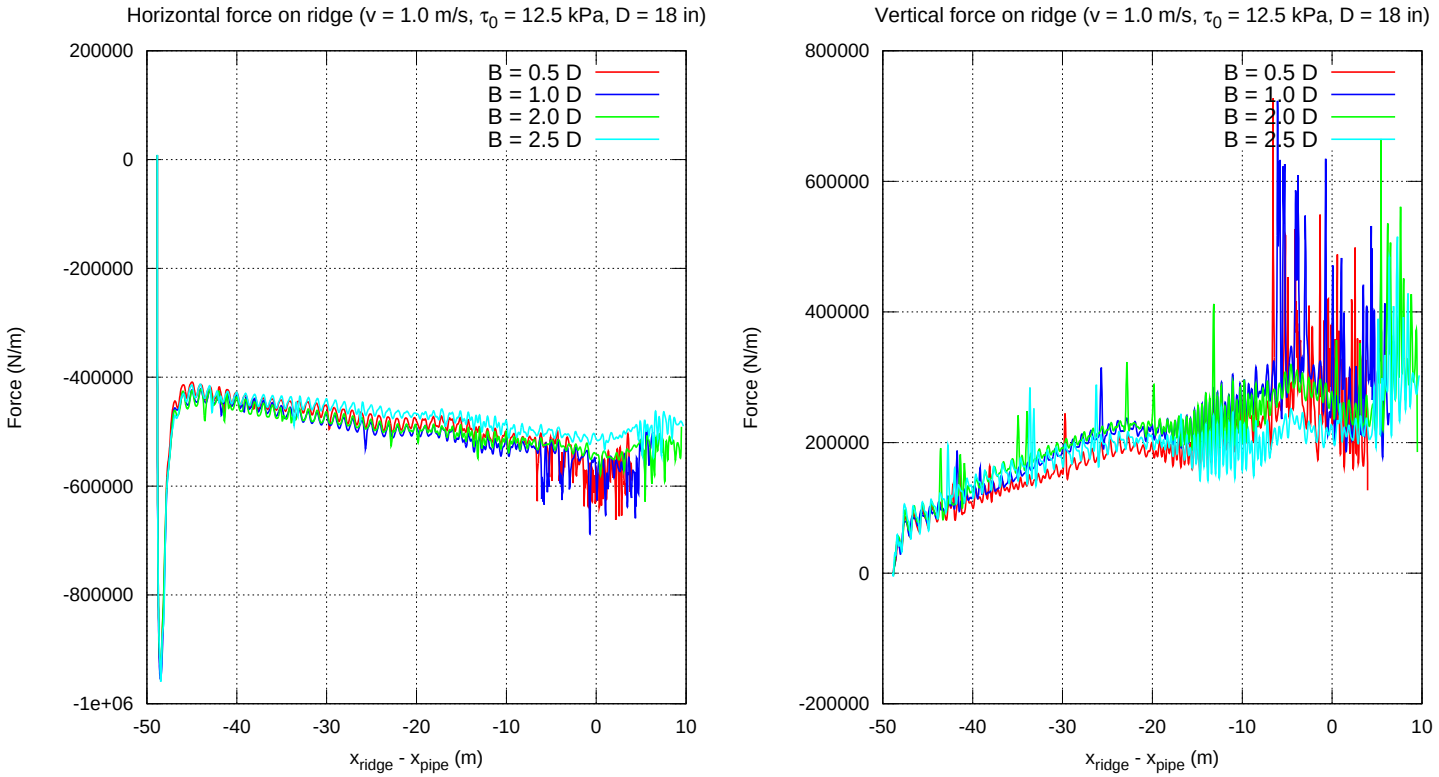

Figure 5.5: Group 2 – Forces acting on ridge

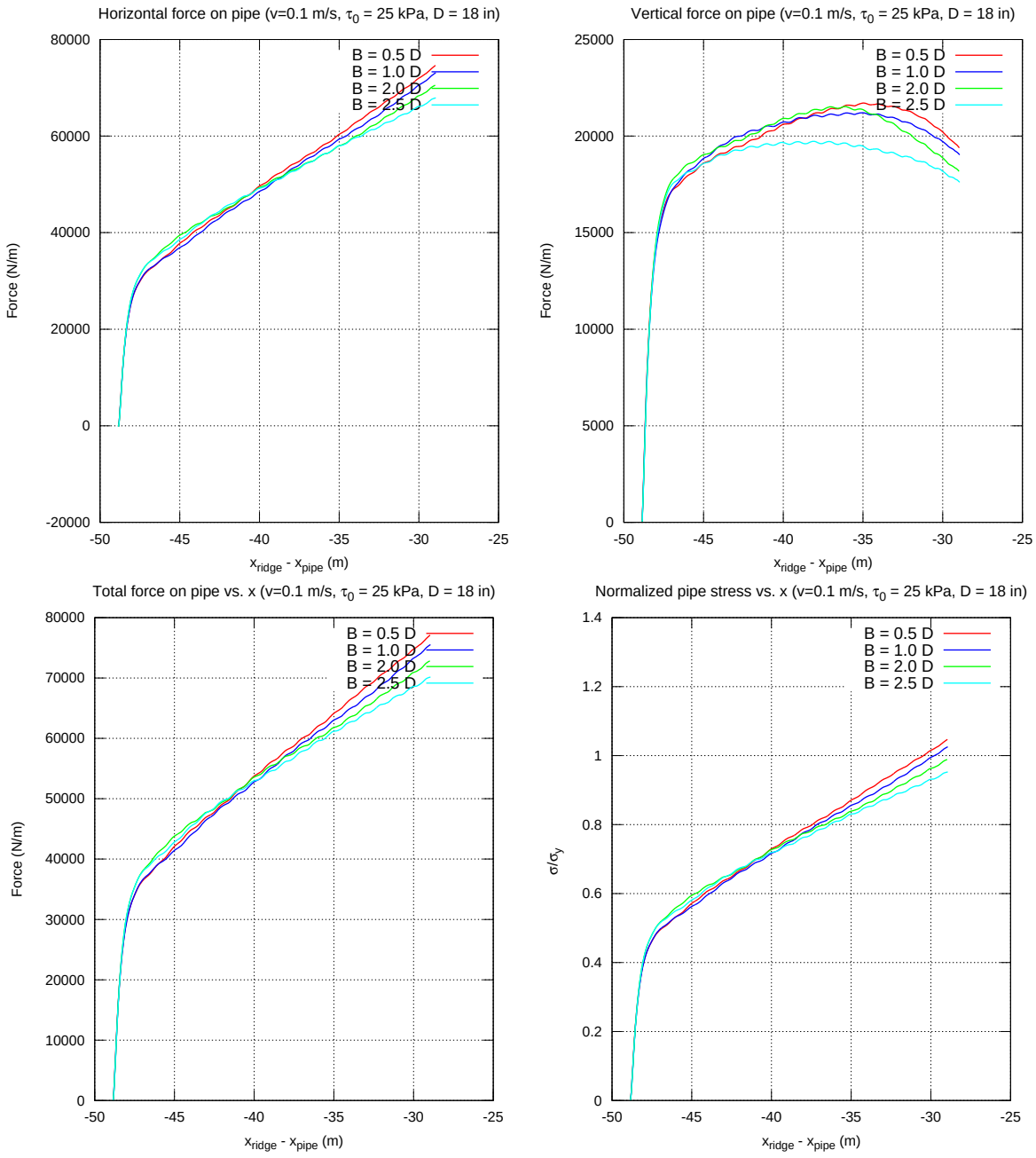

Figure 5.6: Group 3 – Forces and stresses acting on pipe.

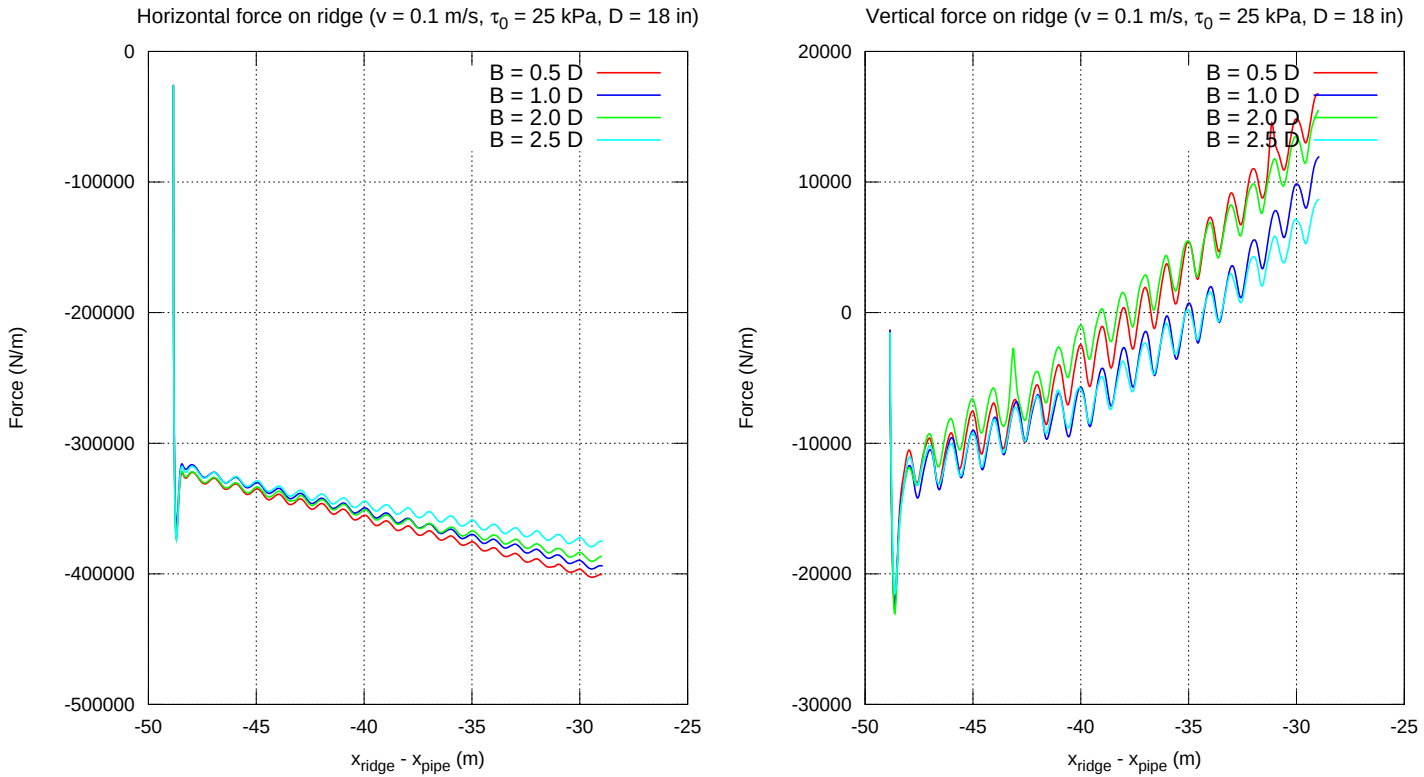

Figure 5.7: Group 3 – Forces acting on ridge.

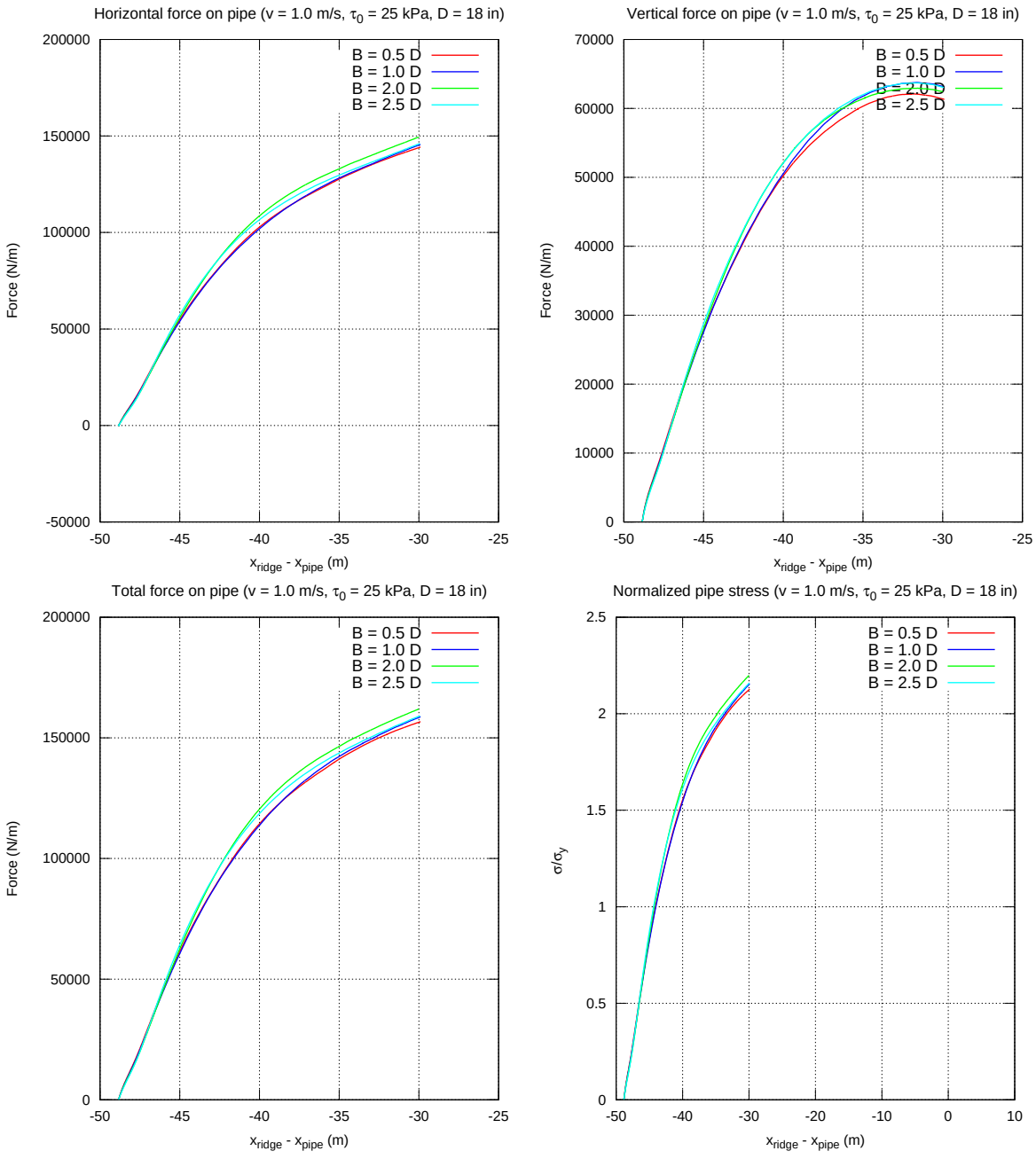

Figure 5.8: Group 4 – Forces and stresses on pipe.

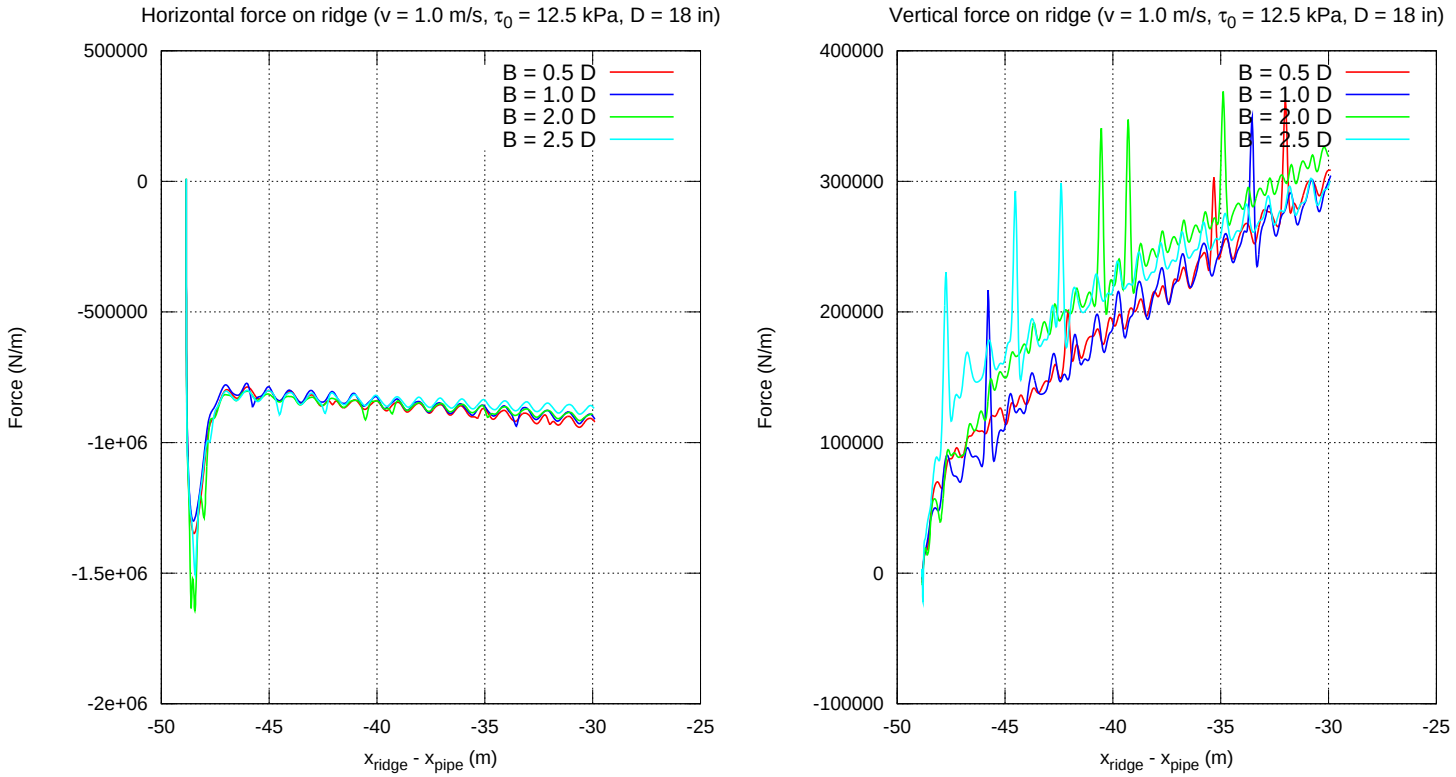

Figure 5.9: Group 4 – Forces acting on ridge.

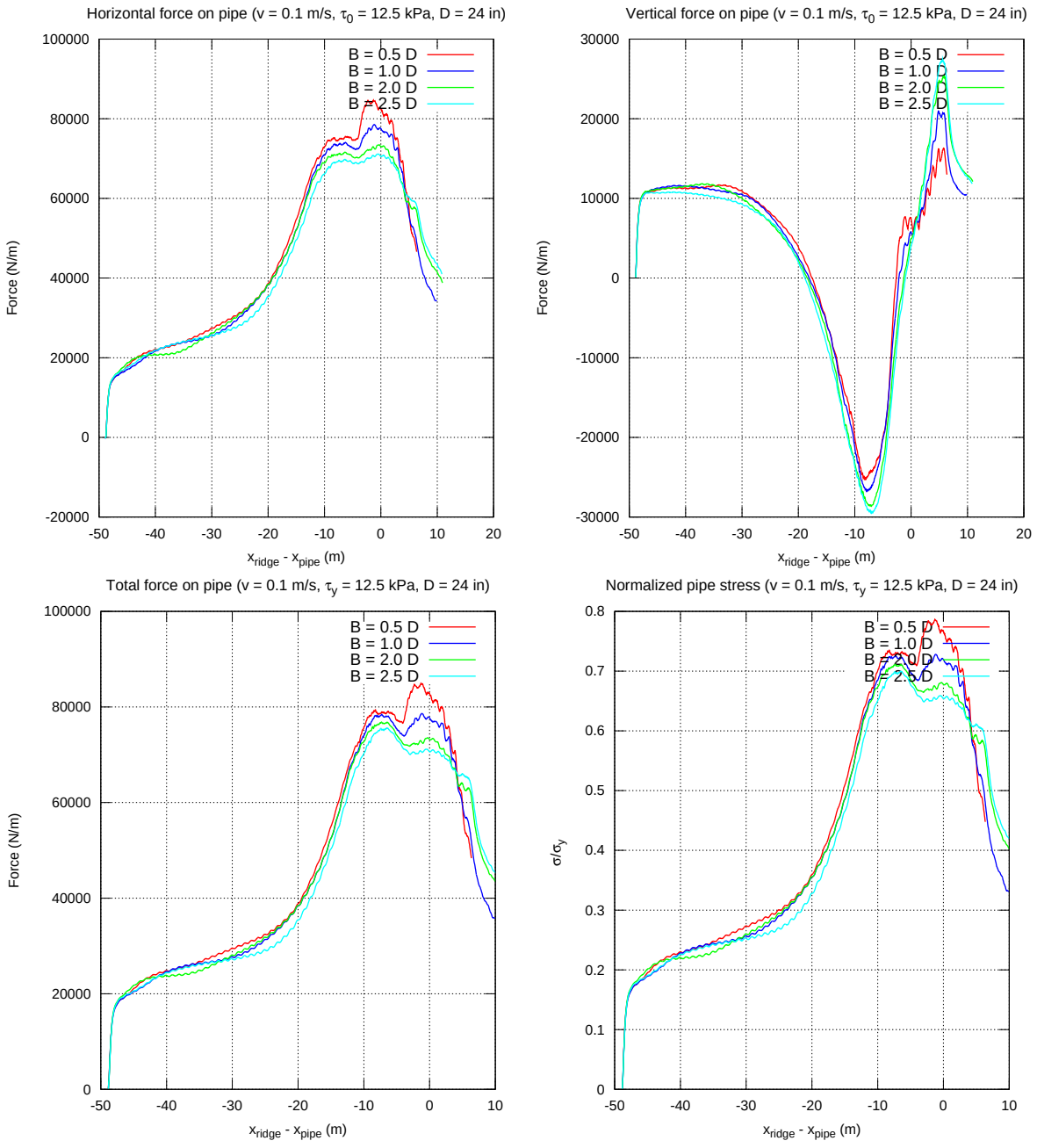

Figure 5.10: Group 5 – Forces and stresses acting on pipe.

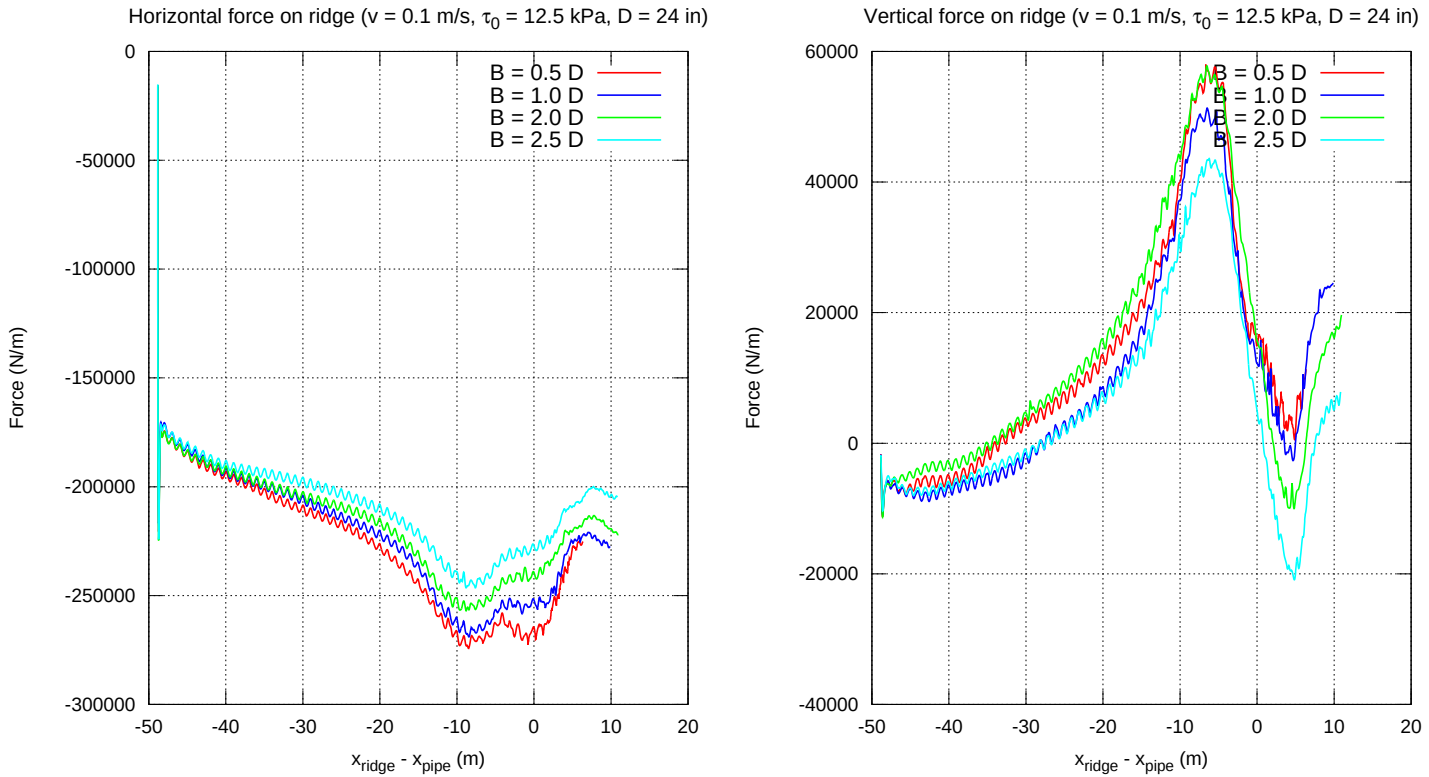

Figure 5.11: Group 5 – Forces acting on ridge.

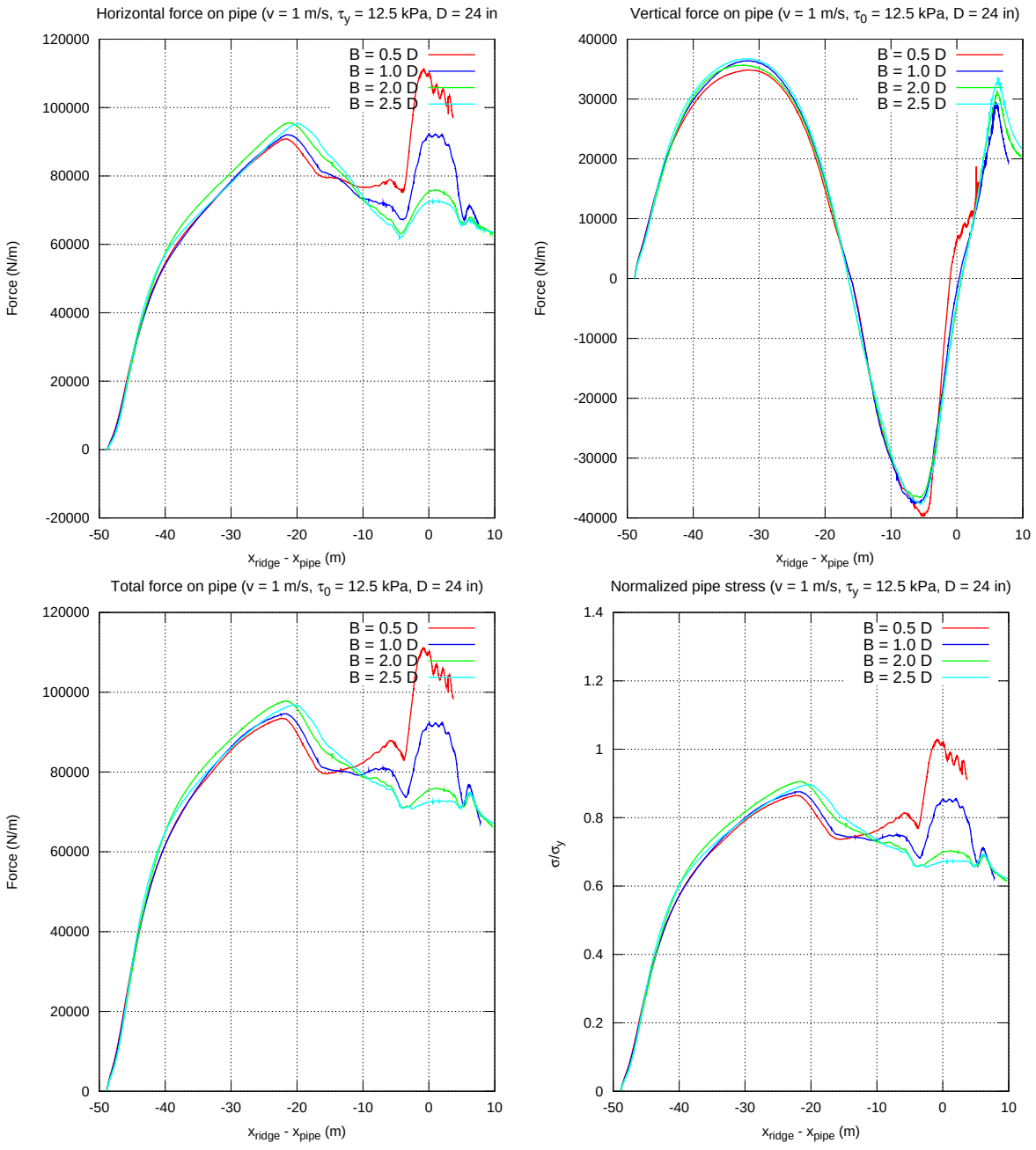

Figure 5.12: Group 6 – Forces and stresses acting on pipe.

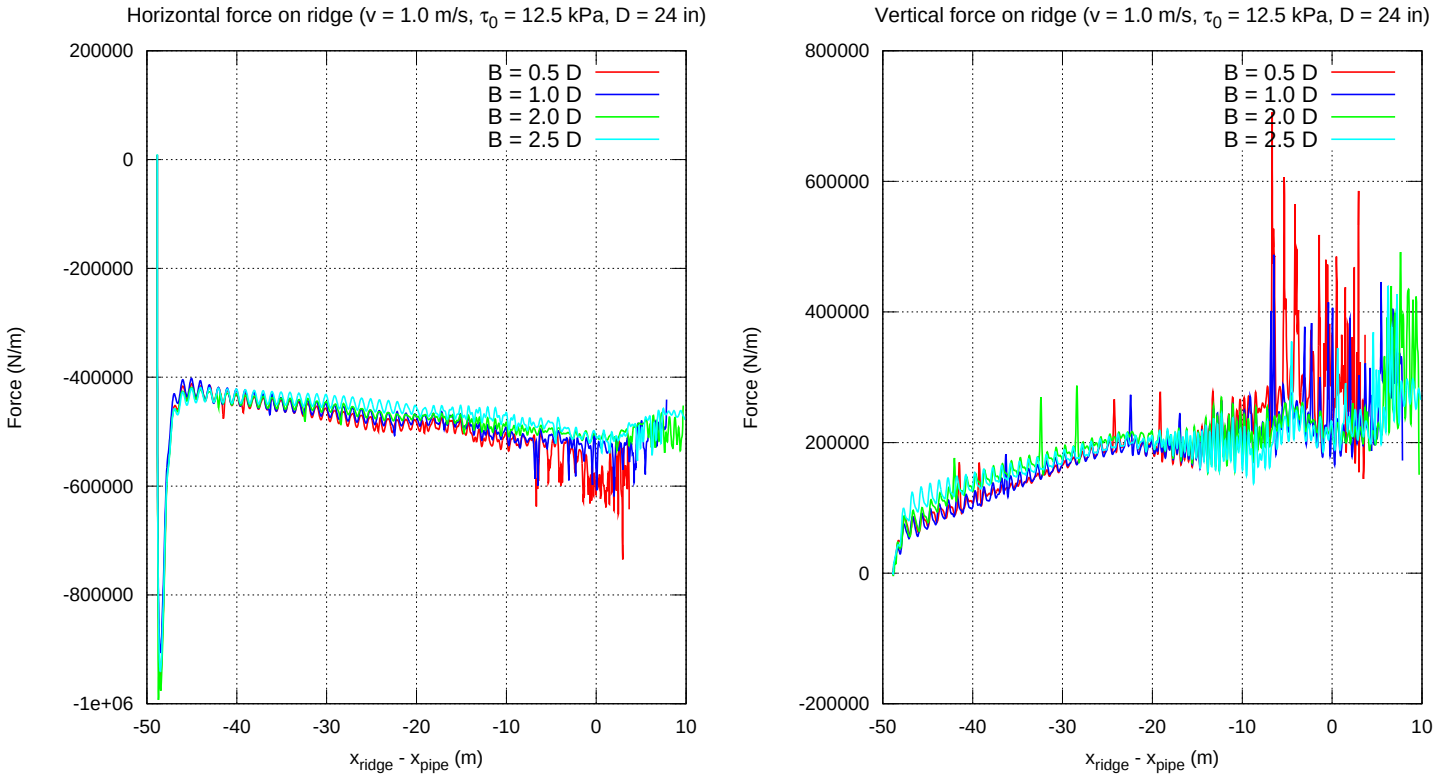

Figure 5.13: Group 6 – Forces acting on ridge.

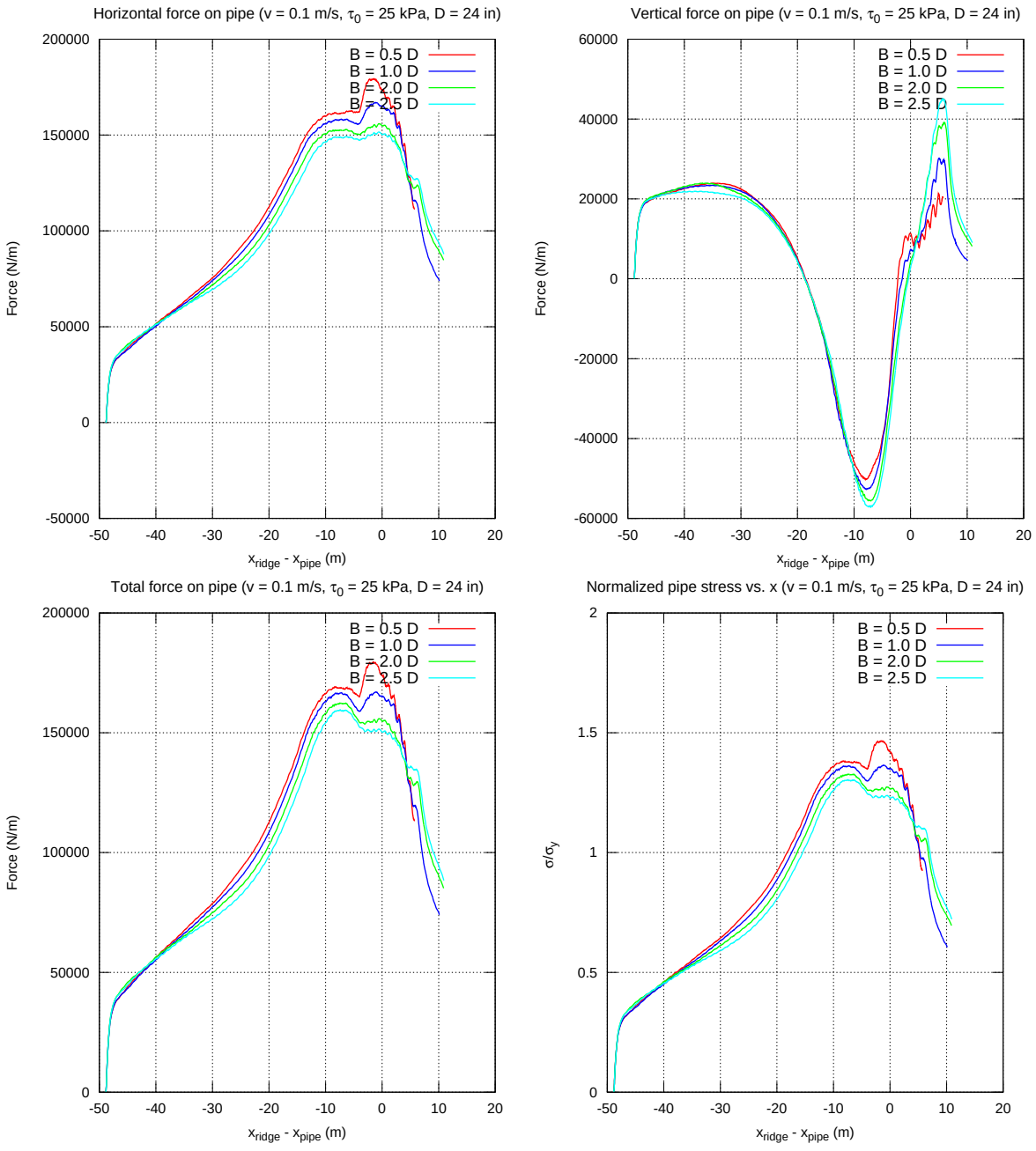

Figure 5.14: Group 7 – Forces and stresses on pipe.

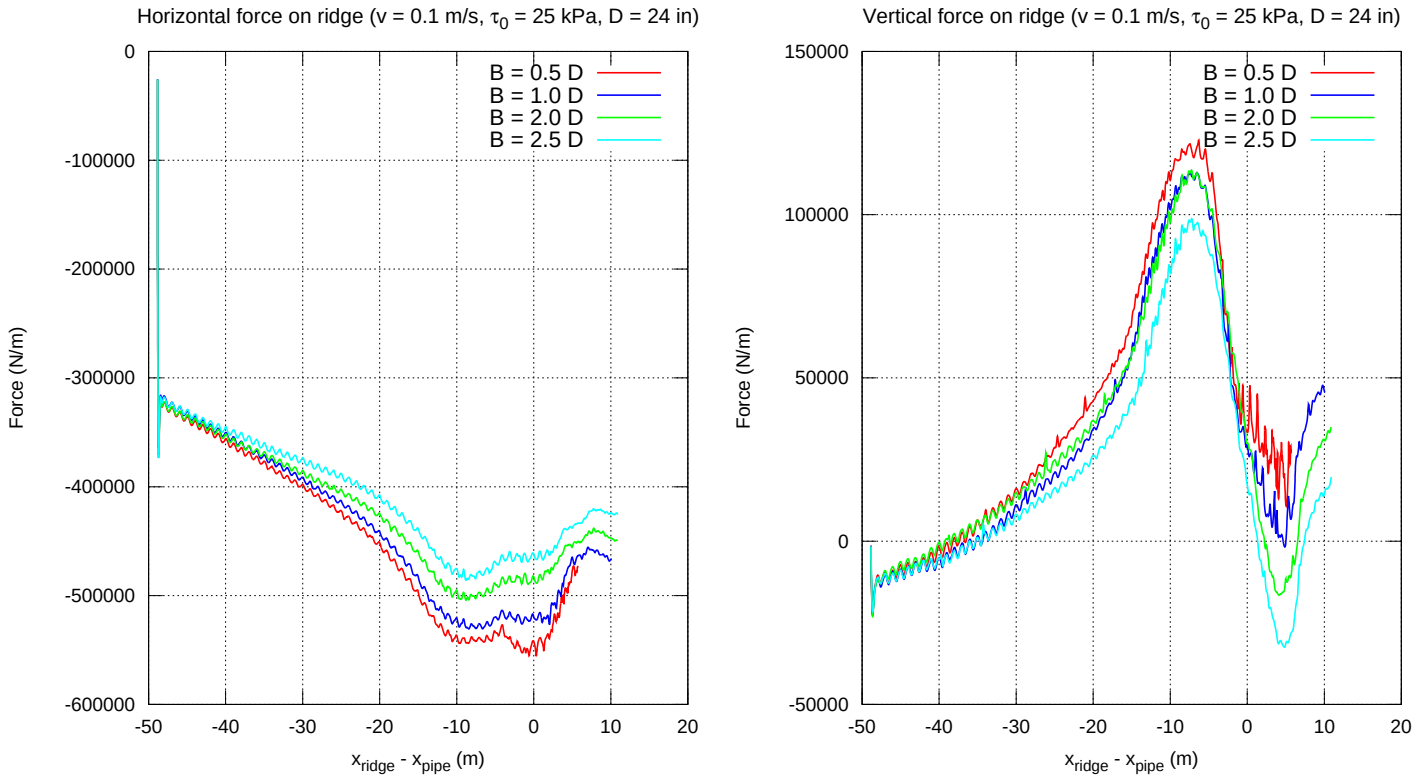

Figure 5.15: Group 7 – Forces on ridge.

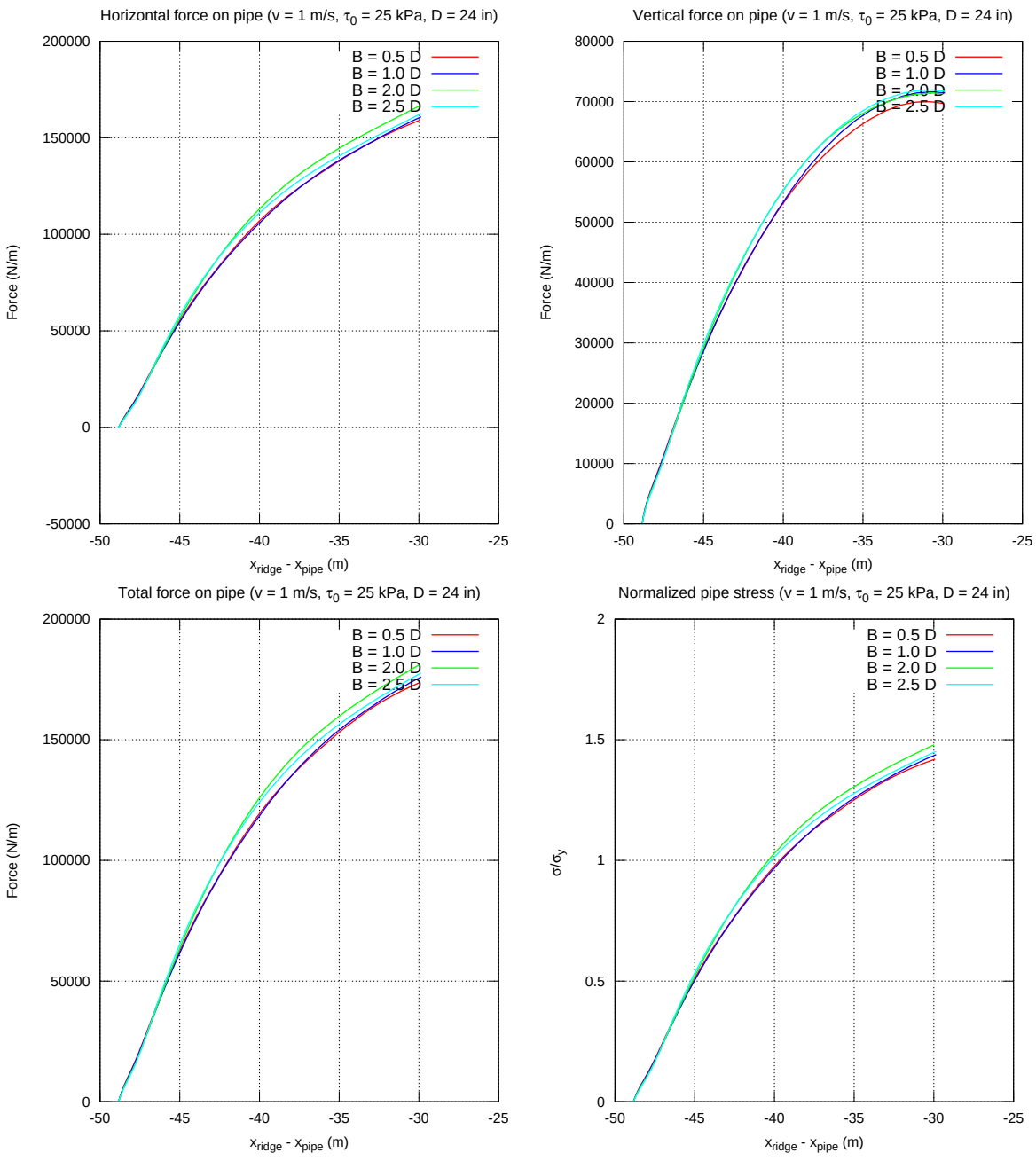

Figure 5.16: Group 8 – Forces and stresses on pipe.

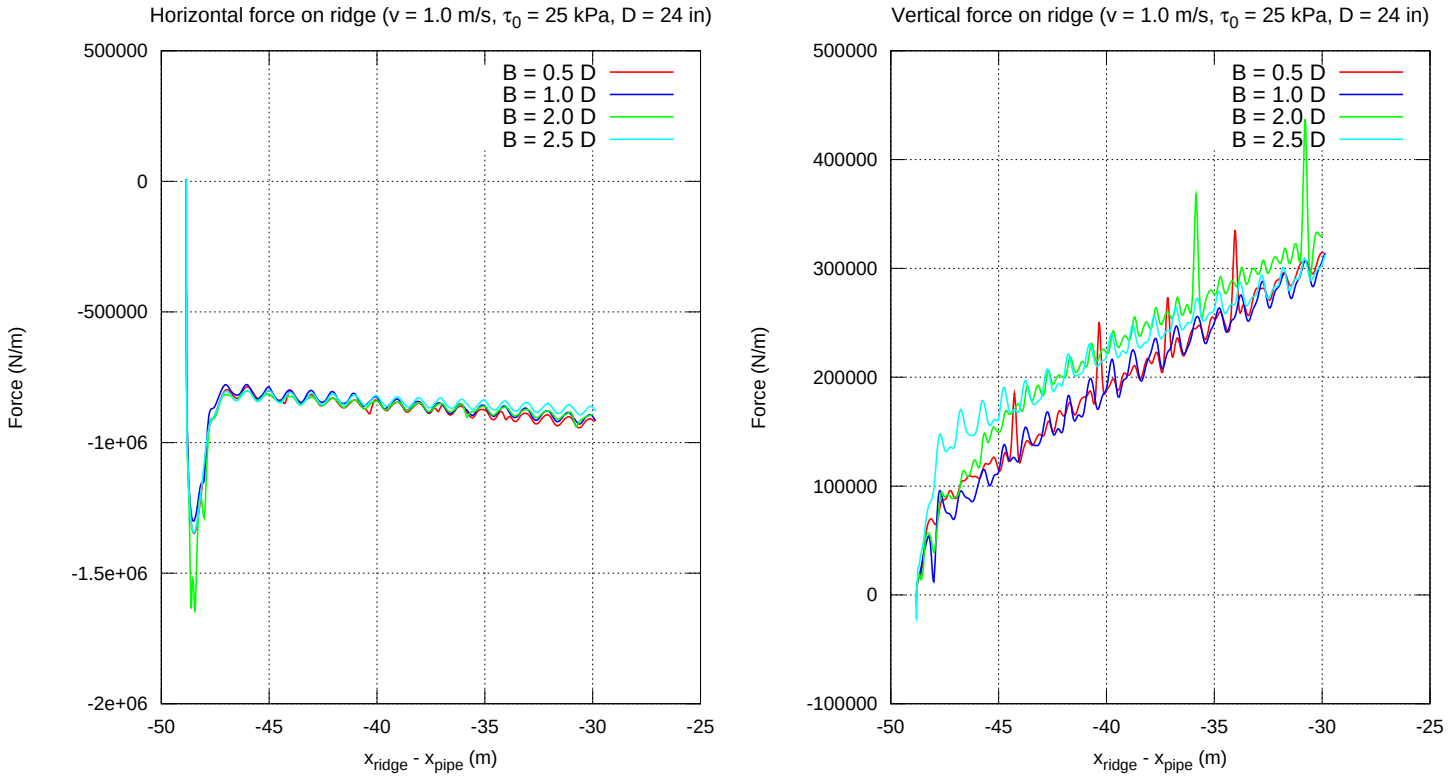

Figure 5.17: Group 8 – Forces on ridge.

The components of the ridge forces for Group 7 are shown in Figure 5.15. Assuming out-of-plane lengths of 10 meters, consistent with the base of the ridge, the horizontal component of the ridge is in good agreement with those show in Figure 6 in [23].

The maximum lateral pipe displacement of 0.36 meters in Group 7 for a pipe with a clearance of 1 pipe diameter is comparable to the maximum transverse displacement of ≈ 0.3 meters obtained in the Wrinkler-type quasistatic analysis performed in [23] with same soil strength. The maximum Von Mises stress in the same study was determined to be roughly 320 MPa from a Wrinkler-type analysis, and roughly 260 MPa using the continuum approach described in the same paper. Our results for Group 7 (1 pipe diameter clearance) predict a maximum stress of 490 MPa.

Finally, the typical seabed profiles at various times for Groups 5, 6, and 7 are shown in Figures 5.18, 5.19, and 5.20, respectively. These results indicate that the mound formed in front of the ridge is sensitive to both the soil strength and ridge speed.

6 3-Dimensional Gouging

Using the same constitutive model, we consider the gouging of seabed in three-dimensions by a square indentor in absence of a buried pipe. The computational domain is a closed rectangular box, with no-slip conditions imposed on all walls. The indentor is taken to be cube-shaped with no-slip boundary conditions on its sides. No pipeline is included in this analysis.

Figure 6.1 shows the profile of the seabed after gouging from various angles. The qualitative form of the trench created and the side and front mounds are in agreement with those obtained using classical CSM analysis.

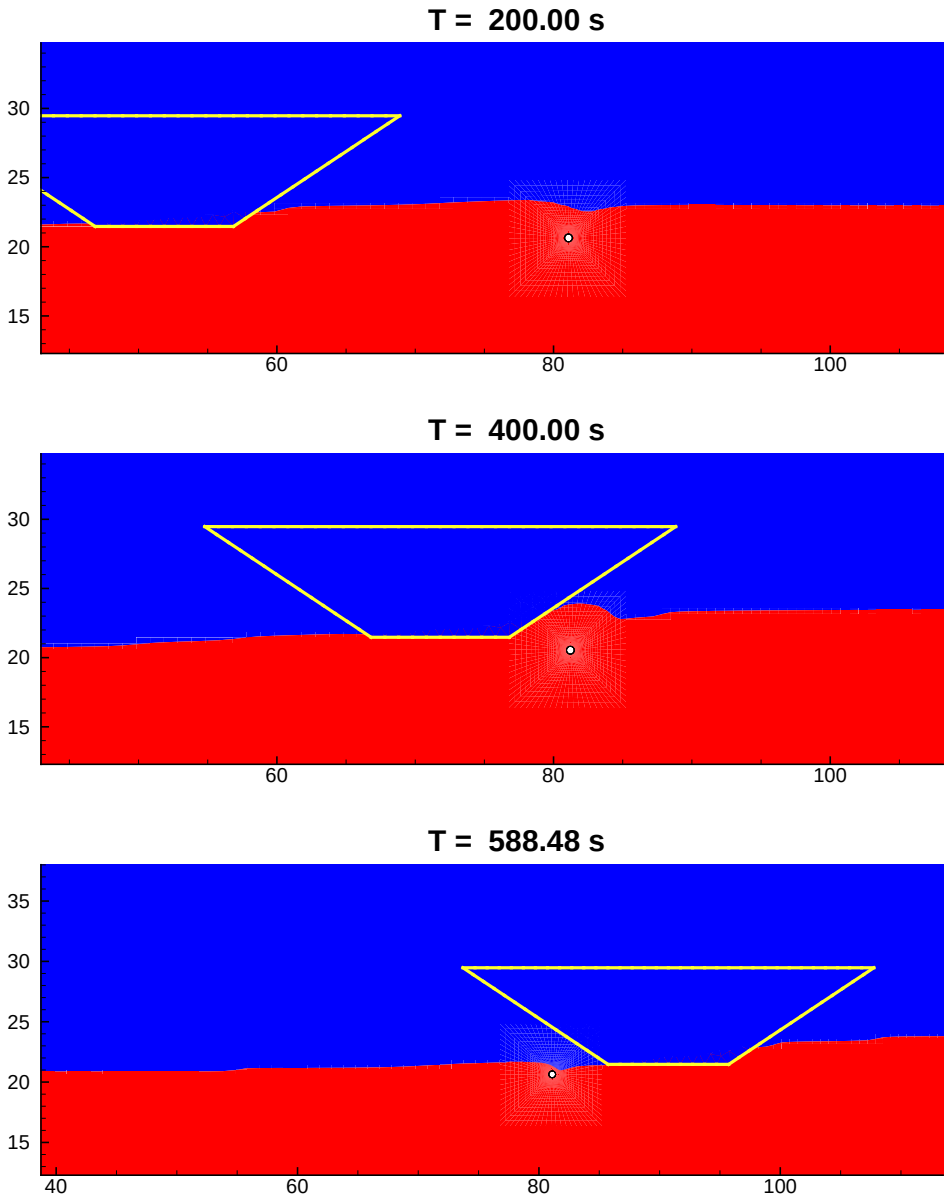

Figure 5.18: Snapshots of the estimated seabed profile for Group 5, $B = 1D$.

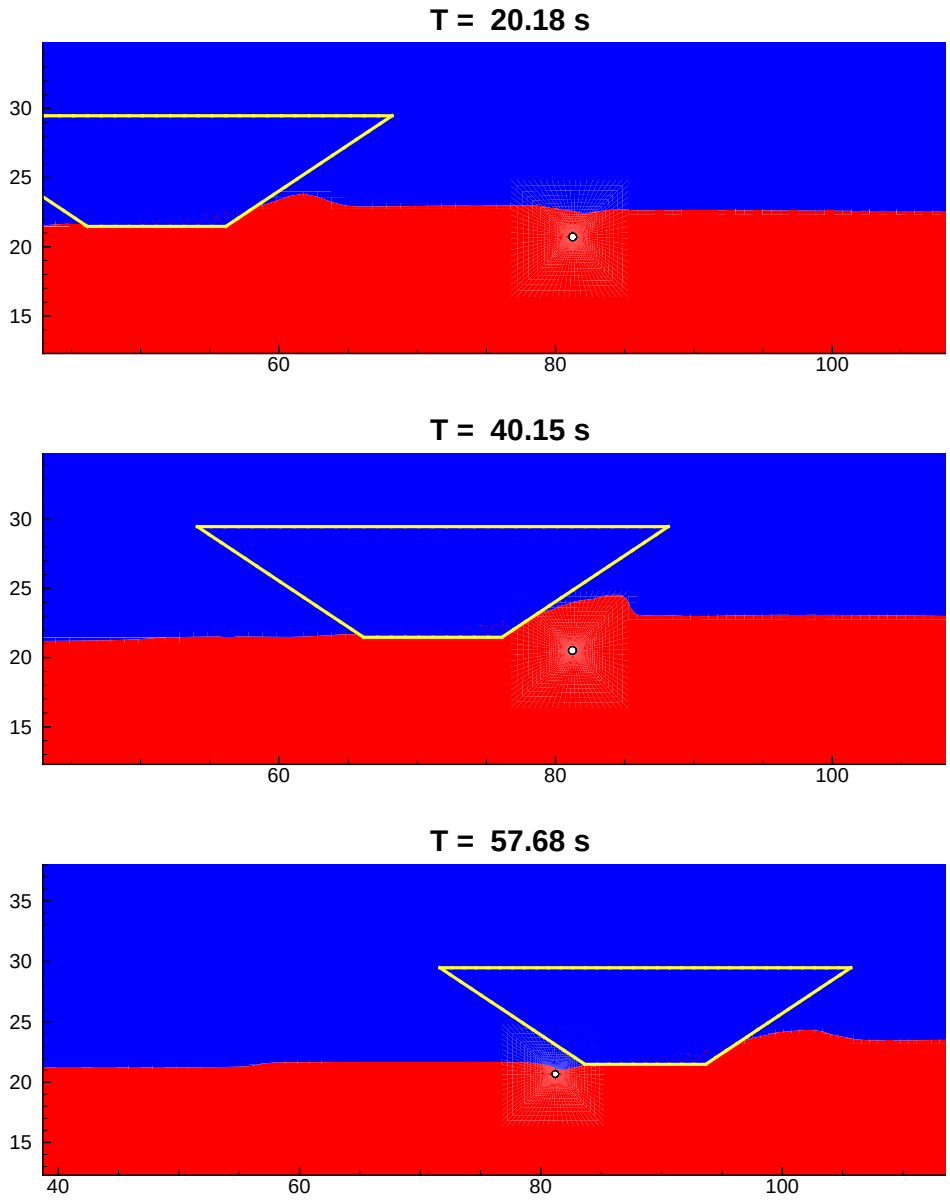

Figure 5.19: Snapshots of the estimated seabed profile for Group 6, $B = 1D$.

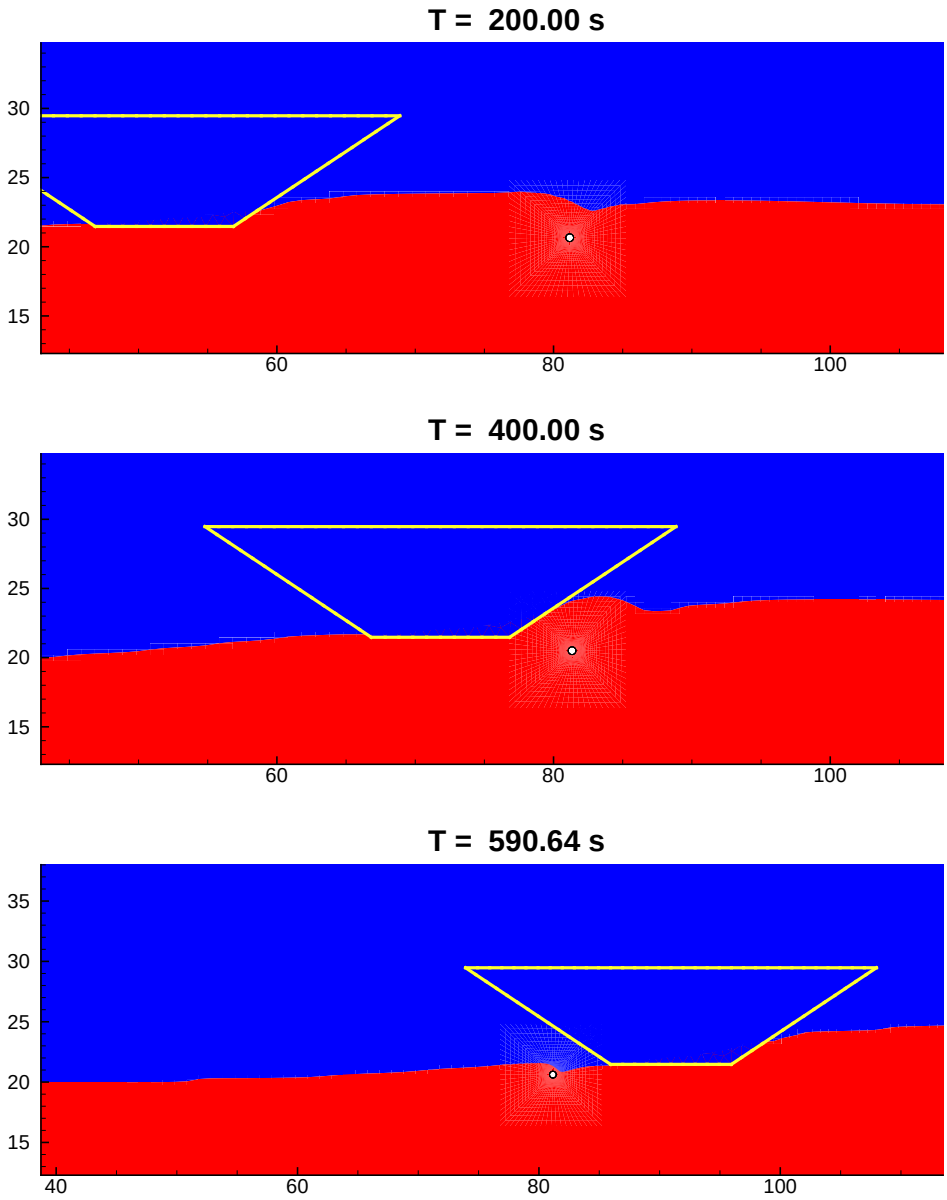

Figure 5.20: Snapshots of the estimated seabed profile for Group 7, $B = 1D$.

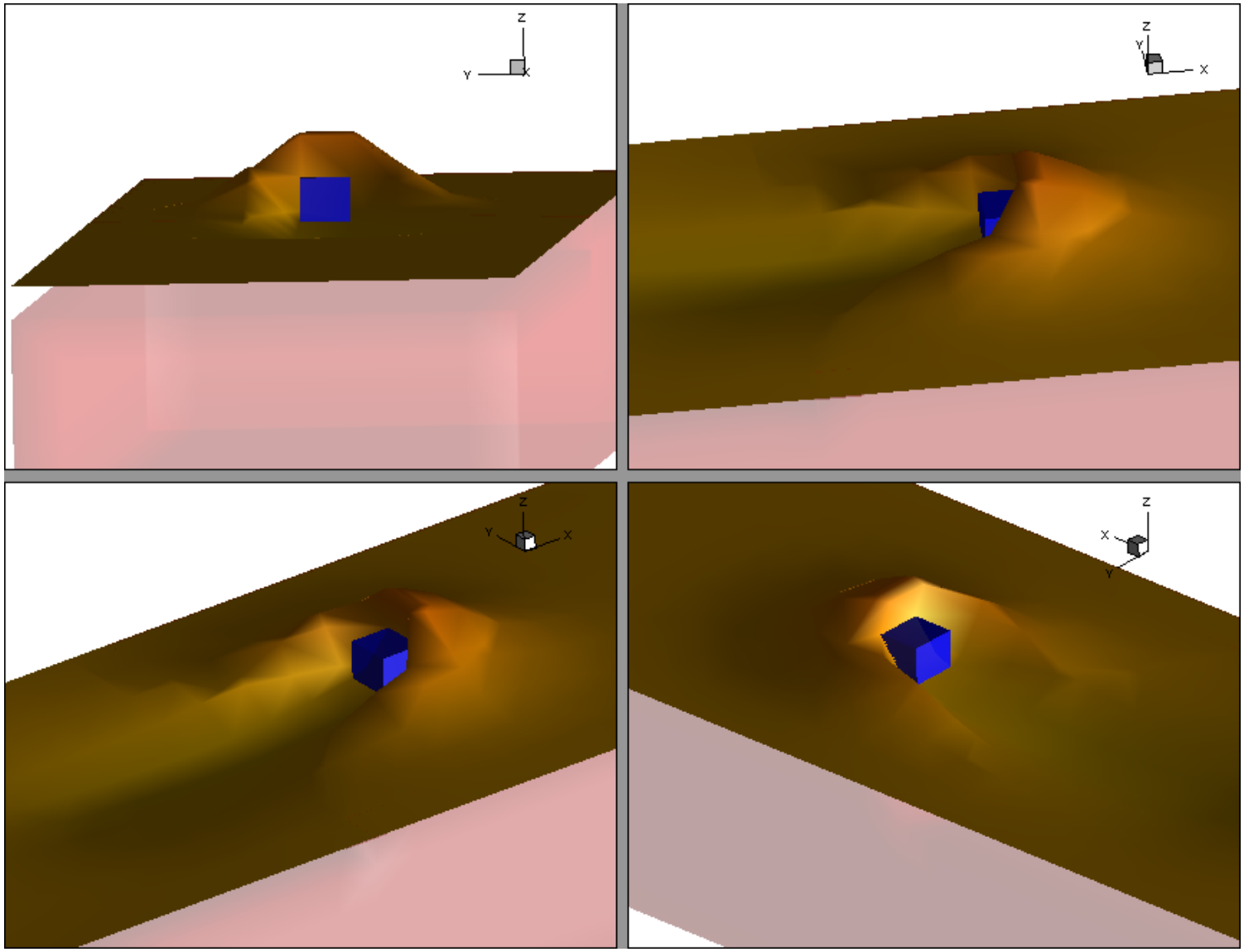

Figure 6.1: Seabed scour profile after scour by a rigid cube-shaped indentor.

7 Observations and Conclusions

This study presents a novel approach of treating soil as an incompressible viscous fluid to conduct seabed scour analysis and gain insight in to the coupled ridge-soil-pipe interaction analysis. Treating the soil as a viscous fluid while capturing the soil profile facilitates computation of the very large topological changes in the seabed without the need for computationally expensive remeshing.

Some of the observations from the analysis carried out in this study are as follows:

1. Higher ridge speeds result in higher pipe stresses (for instance, 25% increase in stresses from Group 5 to Group 6).
2. Increase in loading rate has a bigger effect in subgouge forces for soils with higher soil strength.
3. Increase in soil strength results in much larger forces on the pipe as pointed out in [23].
4. Soil strength and ridge speed play a big role in size and shape of the soil mound formed in front of the ridge.
5. For soil strengths of 12.5 kPa, pipelines 18-inches in diameter are susceptible to yielding (52 ksi steel) with as much as 2.5 pipe-diameter clear distance to base of ridge (Groups 1 and 2).
6. For soil strengths of 12.5 kPa and ridge speeds of 0.1 m/s, pipelines 24-inches in diameter are deemed safe from yielding (52 ksi steel) with clear distances as low as 0.5 pipe diameter (Group 5).
7. For soil strengths of 12.5 kPa and extreme ridge speeds of 1 m/s, pipelines 24-inches in diameter require minimum clear distance of one pipe diameter (Group 6, see Figure 5.12) to be safe from yielding.
8. Both 18- and 24-inch pipe diameters are susceptible to yielding (52 ksi steel) in soil strengths of 25 kPa even with clear distances as much as 2.5 pipe-diameters.

Cases considered in this study which are comparable to the full-blown three-dimensional analysis done in [23] are in agreement. There is a need to further validate these numerical results through experimental data obtained through centrifuge tests, reduced-scale laboratory and in-situ testing.

References

[1] Barker A. and Timco G. Laboratory experiments of ice scour processes: rigid ice indentor. *Cold Regions Science and Technology*, 35(3):195–206, 2002.

[2] Paul Barrette. Offshore pipeline protection against seabed gouging by ice: An overview. *Cold Regions Science and Technology*, 69(1):3 – 20, 2011.

[3] D.W. Bass and C. Woodworth-Lynas. Iceberg crater marks on the sea floor, labrador shelf. *Marine Geology*, 79(3-4):243 – 260, 1988.

[4] Y. Bazilevs, V.M. Calo, T.J.R. Hughes, and Y. Zhang. Isogeometric fluid-structure interaction: theory, algorithms, and computations. *Computational Mechanics*, 43:3–37, 2008.

[5] Eddy Carmack and Robie Macdonald. Oceanography of the canadian shelf of the beaufort sea: A setting for marine life. *ARCTIC*, 55(5), 2002.

[6] T. Ramanuja Chari. Geotechnical aspects of iceberg scours on ocean floors. *Canadian Geotechnical Journal*, 16(2):379–390, 1979.

[7] D. L. Gautier, K. J. Bird, R. R. Charpentier, A. Grantz, D. W. Houseknecht, T. R. Klett, J. K. Moore, T. E.and Pitman, C. J. Schenk, J. H. Schuenemeyer, K. Sorensen, M. E. Tennyson, Z. C. Valin, and C. J. Wandrey. Assessment of undiscovered oil and gas in the arctic. *Science*, 324:1175 – 1179, 2009.

[8] Somnath Ghosh and Noboru Kikuchi. An arbitrary lagrangian-eulerian finite element method for large deformation analysis of elastic-viscoplastic solids. *Computer Methods in Applied Mechanics and Engineering*, 86(2):127 – 188, 1991.

[9] Francis H. Harlow. The particle-in-cell computing method for fluid dynamics. *Methods Comput. Phys.*, 3:319–343, 1964.

[10] Arnaud Héquette, Marc Desrosiers, and Peter W. Barnes. Sea ice scouring on the inner shelf of the southeastern canadian beaufort sea. *Marine Geology*, 128(3-4):201 – 219, 1995.

[11] C.W Hirt, A.A Amsden, and J.L Cook. An arbitrary lagrangian-eulerian computing method for all flow speeds. *Journal of Computational Physics*, 14(3):227 – 253, 1974.

[12] Thomas J.R. Hughes, Wing Kam Liu, and Thomas K. Zimmermann. Lagrangian-eulerian finite element formulation for incompressible viscous flows. *Computer Methods in Applied Mechanics and Engineering*, 29(3):329 – 349, 1981.

[13] Tony King, Ryan Phillips, John Barrett, and Gary Sonnichsen. Probabilistic pipeline burial analysis for protection against ice scour. *Cold Regions Science and Technology*, 59(1):58 – 64, 2009.

[14] Ibrahim Konuk and Robert Gracie. A 3-dimensional eulerian finite element model for ice scour. *ASME Conference Proceedings*, 2004(41766):1911–1918, 2004.

[15] Ibrahim Konuk and Shenkai Yu. A pipeline case study for ice scour design. *ASME Conference Proceedings*, 2007(42711):163–169, 2007.

[16] Pavel Liferov and Knut V. Hyland. In-situ ice ridge scour tests: experimental set up and basic results. *Cold Regions Science and Technology*, 40(1-2):97 – 110, 2004.

[17] D.C. Lo and D.L. Young. Arbitrary lagrangian-eulerian finite element analysis of free surface flow using a velocityvorticity formulation. *Journal of Computational Physics*, 195(1):175 – 201, 2004.

[18] C. M. Martin and M. F. Randolph. Upper-bound analysis of lateral pile capacity in cohesive soil. *Geotechnique*, 56:141–145, 2006.

[19] R. Merifield, D. White, and M. Randolph. Effect of surface heave on response of partially embedded pipelines on clay. *Journal of Geotechnical and Geoenvironmental Engineering*, 135(6):819–829, 2009.

[20] R. Merifield, D. J. White, and M. F. Randolph. The ultimate undrained resistance of partially embedded pipelines. *Geotechnique*, 58:461–470, 2008.

[21] J.M.G. Miller, E.W. Domack, N. Eyles, I. Fairchild, and G.M. Young. *Earth's Glacial Record*. World and Regional Geology. Cambridge University Press, 2004.

[22] J. D. Murff, D. A. Wagner, and M. F. Randolph. Pipe penetration in cohesive soil. *Geotechnique*, 39:213–229, 1989.

[23] A. Nobahar, S. Kenny, and R. Phillips. Buried pipelines subject to subgouge deformations. *International Journal of Geomechanics*, 7(3):206–216, 2007.

[24] A.C. Palmer and R.A. King. *Subsea Pipeline Engineering, 2E.* PennWell, 2008.

[25] A.C. Palmer, I. Konuk, G. Comfort, and K. Been. Ice gouging and the safety of marine pipelines. *Offshore Technology Conference*, pages 235–244, 1990.

[26] Andrew Palmer. Geotechnical evidence of ice scour as a guide to pipeline burial depth. *Canadian Geotechnical Journal*, 34(6):1002–1003, 1997.

[27] R. Peek and A. Nobahar. Ice gouging over a buried pipeline: Superposition error of simple beam-and-spring models. *International Journal of Geomechanics*, 12(4):508–516, 2012.

[28] M. Raie and J. Tassoulas. Installation of torpedo anchors: Numerical modeling. *Journal of Geotechnical and Geoenvironmental Engineering*, 135(12):1805–1813, 2009.

[29] M. F. Randolph and G. T. Houlsby. The limiting pressure on a circular pile loaded laterally in cohesive soil. *Geotechnique*, 34:613–623, 1984.

[30] L.C. Reese and W.F. Van Impe. *Single Piles and Pile Groups Under Lateral Loading*. Balkema, 2001.

[31] Antonio Rodríguez-Ferran, Agustí Pérez-Foguet, and Antonio Huerta. Arbitrary lagrangianeulerian (ale) formulation for hyperelastoplasticity. *International Journal for Numerical Methods in Engineering*, 53(8):1831–1851, 2002.

[32] Mohamed Sayed and Garry W. Timco. A numerical model of iceberg scour. *Cold Regions Science and Technology*, 55(1):103 – 110, 2009.

[33] M. Souli and J.P. Zolesio. Arbitrary lagrangianeulerian and free surface methods in fluid mechanics. *Computer Methods in Applied Mechanics and Engineering*, 191(3-5):451 – 466, 2001.

[34] D. G. True. *Undrained vertical penetration into ocean bottom soils*. dissertation, University of California at Berkley, 1976.

[35] P. Wadhams. *Ice in the Ocean*. CRC PressINC, 2000.

[36] D. J. White, C. Gaudin, and H. R.C. Dingle. Mechanisms of pipe embedment and lateral breakout on soft clay. *Canadian Geotechnical Journal*, 45(5):636–652, 2008.

[37] Thomas Wick. Fluid-structure interactions using different mesh motion techniques. *Computers & Structures*, 89(13-14):1456 – 1467, 2011.